Southern Hemisphere extra-tropical forcing: a new paradigm for El Niño-Southern Oscillation

Pascal Terray

Southern Hemisphere extra-tropical forcing:

A new paradigm for El Niño-Southern Oscillation

Pascal Terray[1]

LOCEAN/IPSL, CNRS/IRD/UPMC/MNHN, Paris, France

submitted to **Climate Dynamics**

Revised 19 March 2010

[1] Corresponding author address : Pascal Terray, LOCEAN-IPSL, Université Pierre et Marie Curie, BP100 – 4 place Jussieu, 75252 Paris cedex 05, France.
Tel : +33 1 44 27 70 78
E-mail : terray@locean-ipsl.upmc.fr

ABSTRACT

The main goal of this paper is to shed additional light on the reciprocal dynamical linkages between mid-latitude Southern Hemisphere climate and the El Niño-Southern Oscillation (ENSO) signal.

While our analysis confirms that ENSO is a dominant source of interannual variability in the Southern Hemisphere, it is also suggested here that subtropical dipole variability in both the southern Indian and Atlantic Oceans triggered by Southern Hemisphere mid-latitude variability may also provide a controlling influence on ENSO in the equatorial Pacific. This subtropical forcing operates through various coupled air-sea feedbacks involving the propagation of subtropical SST anomalies into the deep tropics of the Atlantic and Indian Oceans from boreal winter to boreal spring and a subsequent dynamical atmospheric response to these SST anomalies linking the three tropical basins at the beginning of the boreal spring. This atmospheric response is characterized by a significant weakening of the equatorial Atlantic and Indian Inter-Tropical Convergence Zone (ITCZ). This weakened ITCZ forces an equatorial "cold Kelvin wave" response in the middle to upper troposphere that extends eastward from the heat sink regions into the western Pacific. By modulating the vertical temperature gradient and the stability of the atmosphere over the equatorial western Pacific Ocean, this Kelvin wave response promotes persistent zonal wind and convective anomalies over the western equatorial Pacific, which may trigger El Niño onset at the end of the boreal winter. These different processes explain why South Atlantic and Indian subtropical dipole time series indices are highly significant precursors of the Niño34 SST index several months in advance before the El Niño onset in the equatorial Pacific.

This study illustrates that the atmospheric internal variability in the mid-latitudes of the Southern Hemisphere may significantly influence ENSO variability. However, this surprising relationship is observed only during recent decades, after the so-called 1976/77 climate regime shift, suggesting a possible linkage with global warming or decadal fluctuations of the climate system.

Keywords: ENSO; Southern Hemisphere; long-range predictability; ocean-atmosphere interactions.

1. Introduction

El Niño-Southern Oscillation (ENSO) phenomenon originates in the tropical Pacific Ocean and oscillates between warm and cold episodes with a rough periodicity of three to seven years (Chang et al., 2006). ENSO events have significant impacts on global weather variability through changes in tropical Pacific convection patterns which excite atmospheric Rossby waves that propagate to higher latitudes (Trenberth et al., 1998; Alexander et al., 2002). For these reasons, considerable effort has been devoted to predict Sea Surface Temperature (SST) in the tropical Pacific several seasons in advance (e.g. Clarke and Van Gorder, 2003; McPhaden et al., 2006; Sara et al., 2006; Jin et al. 2008). However, successful seasonal ENSO prediction remains particularly challenging with skills hampered by the inability of the current systems to correctly predict both the timing and amplitude of ENSO events through the so-called spring predictability barrier in the tropical Pacific. In other words, the evolution and strength of ENSO events are very difficult to predict before their onset. This is particularly true for El Niño onsets, which rely on some sort of external forcing (Kessler, 1992) and limit drastically the long-range predictability of ENSO (Chang et al., 2006).

Despite of the large consensus in the literature about the fact that interaction between the atmosphere and ocean within the tropical Pacific basin plays a fundamental role in determining the characteristics of ENSO, there are growing evidences of the possible role of other tropical or extra-tropical oceans in the evolution of ENSO.

During the past decade there has been some effort devoted to identify a possible forcing of the North Pacific Ocean on ENSO (Vimont et al., 2001, 2003, 2009; Anderson, 2003; Chiang and Vimont, 2004; Chang et al., 2007). These studies highlight the possible influence of the North Pacific Oscillation (NPO), a dominant pattern of atmospheric variability in the North Pacific, on the tropical Pacific through the so-called Wind-Evaporation-SST (WES) feedback (e.g. Xie and Philander, 1994; Chang et al., 2006). Following these studies, the NPO-forced subtropical SST anomalies drive zonal wind anomalies over the equatorial Pacific that are responsible of exciting or altering subsequent ENSO events (Vimont et al., 2009).

The tropical Indian Ocean is also known to influence ENSO on intraseasonal to interannual time scales (Yu et al., 2002; Wu and Kirtman, 2004; Annamalai et al., 2005; Kug et al., 2005, 2006; Kug and Kang, 2006; Luo et al., 2009 among many others). Wu and Kirtman (2004) and Kug et al. (2006) found that tropical Indian Ocean SSTs affect ENSO through the modulation of the Pacific and Indian Oceans Walker circulations in their coupled simulations. Furthermore, several studies have demonstrated that Indian Ocean SST anomalies enhance the anomalous anticyclone, which is established over the western North Pacific in the mature phase of El Niño (Watanabe and Jin, 2002; Annamalai et al., 2005; Kug and Kang, 2006). Through the excitation of this anticyclonic pattern that drives easterly wind stress anomalies in the western Pacific, the Indian Ocean SST warming leads to a faster transition to La Niña. More recently, Luo et al. (2009) and Izumo et al. (2010) have also suggested that tropical Indian Ocean Dipole (IOD) events may significantly contribute to the long-range predictability of ENSO.

While numerous studies have been devoted to the influence of the tropical Indian Ocean on ENSO, the Atlantic Ocean has received little attention in this context. Exceptions are the pioneering work of Wright (1986) or the more recent studies of Penland and Matrasova (2006, 2008), Dommenget et al. (2006), Wang (2006), Jansen et al. (2009) and Rodriguez-Fonseca et al. (2009). Using linear inverse modeling, Penland and Matrasova (2006, 2008) find that south tropical Atlantic SSTs precede the El Niño signal by 9 months. Wang (2006) suggests that the tropical Atlantic Ocean acts as a forcing for the equatorial Pacific via the inter-basin SST gradient variability associated with the Atlantic Walker circulation. Similar conclusions have been arrived by Rodriguez-Fonseca et al. (2009) who, however, advocate different physical mechanisms, while Jansen et al. (2009) find that the inclusion of the Atlantic tropical SSTs improves the ENSO forecast skill in their conceptual model. However, the dynamical mechanisms at work for explaining how summer Atlantic tropical SSTs may enhance ENSO events (essentially after the 70's) are far from clear from these studies.

Assuming the tropical Indian and Atlantic Oceans have an influence on ENSO, one may also wonder if the Southern Hemisphere ocean could also have an impact on ENSO. However, there exists not much discussion about the Southern Hemisphere influence on ENSO. On the contrary, numerous studies have documented the significant influence of ENSO on climate variability in the Southern Hemisphere (Karoly, 1989; Kidson and Renwick, 2002; Trenberth et al., 2002; Carleton, 2003). It has even been argued that modes of climate variability in the

higher southern latitudes, such as the Antarctic Circumpolar Wave (ACW) or the Southern Annular Mode (SAM), are remotely controlled or influenced by ENSO (Carril and Navarra, 2001; Kwok and Comiso, 2002; Ribera and Mann, 2003; L'Heureux and Thompson, 2006; Hobbs and Raphael, 2007). Some indications of a Southern Hemisphere influence on ENSO were given, however, in Van Loon and Shea (1987) and a series of works by Peterson and White (1998), White et al. (2002) and White and Annis (2004) using heavily filtered data. Recently, Toniazzo (2009) has also identified a precursor to El Niño in the southeast Pacific using a coupled general circulation model. Moreover, a few recent studies have shown a remarkable change in the lead-lag relationships between Southern Indian Ocean SSTs and ENSO after the 1976/77 climate regime shift (Terray et al., 2005; Terray and Dominiak, 2005). Accordingly, SST anomalies in the southeastern Indian Ocean during boreal winter are key-statistical predictors of ENSO after the climate regime shift (Dominiak and Terray, 2005).

As a complement to the above studies, the present paper explores the possible existence of a Southern Hemisphere extra-tropical forcing of ENSO during recent decades (e.g. after the 1976/77 climate shift). The first goal is to identify the principal modes of variability of the SST and the overlying atmosphere in the mid-latitudes of the Southern Hemisphere at the interannual time scales. A secondary goal is to determine whether these modes of variability may have an impact on the tropical Pacific variability.

This paper is organized as follows. Data and methods are briefly described in Section 2. In Section 3, we first identify the main patterns of uncoupled and coupled variability in the South Pacific, Atlantic and Indian Oceans during austral summer, the main active season for SST variability in the Southern Hemisphere mid-latitudes. We then turn to our main result, the relationships between these patterns of variability and ENSO in Section 4. The conclusions and some discussions are given in Section 5.

2. Data and statistical techniques

a. Data

The principal sources of data used in this study include SST and Sea Level Pressure (SLP) from the Hadley Center analyses (Rayner et al., 2003; Allan and Ansell, 2006), Outgoing Longwave Radiation (OLR) (an indicator of atmospheric convective activity) from the

NOAA Climate Prediction Center (Liebmann and Smith, 1996), and surface heat fluxes derived from the third release of the products of the Objectively Analyzed air-sea Fluxes (OAFlux) project (Yu et al., 2008). While preprocessing of the historical SST and SLP datasets (see below) uses the full period available for each variable (1850-2006 and 1870-2004, respectively), our statistical analyses cover only the recent decades, after the 1976/77 climate regime shift, when satellite estimates are available. We also use wind (at various levels), SLP, and 200 hPa streamfunction and velocity potential data from the National Center for Environment Prediction-National Center for Atmospheric Prediction (NCEP-NCAR) reanalysis (Kalnay et al. 1996). Qualitatively similar results are obtained by use of the other historical reconstructions, the European Centre for Medium Range Weather Forecasts (ECMWF) reanalysis (Uppala et al. 2005) or the NCEP2 reanalysis (Kanamitsu et al., 2002), but we only show results from the NCEP-NCAR reanalysis in this paper. Bi-monthly time series are computed for all the fields prior to further processing.

Finally, the Niño34 SST anomaly time series is used as an indicator of the ENSO variability in the tropical Pacific. As usual, the Niño34 index is defined as the SST anomalies averaged in the eastern equatorial Pacific over the domain 5°S-5°N and 170°-120°W.

b. Methods

The annual cycle, trends and very low-frequency variations were removed from the historical SST and SLP bi-monthly fields using the STL (Seasonal-Trend decomposition procedure based on Loess) additive scheme developed by Cleveland et al. (1990). The STL procedure is a powerful statistical technique for describing a discrete time series (Cleveland et al., 1990). In the STL procedure, the analyzed X_t bi-monthly time series is decomposed into three terms:

$$X_t = T_t + A_t + R_t$$

The T_t term is used to quantify the trend and low-frequency variations in the time series. The A_t term describes the annual cycle and its modulation through time. Finally, the R_t term contains the interannual signal and the noise present in the data. All the terms are estimated through a sequence of applications of locally weighted regression (or loess) to data windows whose length is chosen by the user (Cleveland et al., 1990). The STL procedure is an iterative process, which may be interpreted as a frequency filter directly applicable to non-stationary

time series including harmonic components (Cleveland et al., 1990). Other important features of STL is the specification of the amounts of seasonal and trend smoothing, the ability to produce robust estimates of the trend and seasonal components that are not distorted by aberrant or extreme behavior in the data and the stationarity of the R_t time series. Thus, the STL procedure is particularly useful for extracting the interannual signal from non-stationary and noisy climate observations, as illustrated by Cleveland et al. (1990). The interannual SST and SLP bi-monthly anomalies analyzed here were obtained as the departures from the extracted seasonal cycle, A_t, and trend, $T_{t,}$, components estimated by the STL procedure for each grid-point time series in both the SST and SLP datasets from 1979 to 2006 (2004 for SLP fields). In order to illustrate the effectiveness of the STL procedure to remove both the annual cycle and the very low frequency variability in a time series, Figure 1 shows the power spectra of the raw Niño34 SST bi-monthly time series from 1870 to 2006 and of the average of STL residual components, R_t, of bi-monthly SST time series in the Niño34 region during the same period.

All calculations described below were performed with and without the removal of low-frequency variability by the STL procedure and the main results were similar to the findings described in the next sections. In deed, the STL filtering hardly changes the main patterns of variability of the SST and SLP fields in the Southern Hemisphere during the 1979-2006 period, but increases slightly the fraction of variance these interannual modes explain (not shown).

Empirical Orthogonal Function (EOF) and Singular Value Decomposition (SVD) analyses are used to describe the independent and coupled variability of SST and SLP interannual variability in the Southern Hemisphere. Detailed discussions on EOF and SVD analyses can be found in Bretherton et al. (1992). In all EOF and SVD analyses presented here, the computations are based on temporal covariance matrices weighted by cosine of the latitude so that equal areas carry equal weights. These statistical techniques result in spatial patterns (EOFs and SVDs) and time series. These time series are obtained by projecting the original bi-monthly interannual anomalies onto the EOF or SVD patterns and are called Principal Components (PCs) and Singular Variables (SVs), respectively. The spatial patterns and their associated expansion coefficient time series can be scaled arbitrarily as long as their product remains the same. We adopt here the common scaling such that the time series (PCs or SVs)

have unit variance, so that the associated spatial patterns represent a typical anomaly pattern associated with one standard deviation of the expansion coefficient time series.

Finally, standard regression and correlation analyses have been used to describe the life cycle of coupled patterns of variability in the Southern Hemisphere. Note that none of the fields used in these regression exercises were filtered by the STL procedure in order to give an exact overview of the ENSO long-range predictability associated with interannual variability in the Southern Hemisphere. To account for the effects of autocorrelation, the statistical significance levels for these correlation and regression coefficients have been estimated using the method proposed by Ebisuzaki (1997) with 999 samples.

c. Description of SST interannual variability

Figure 2 displays the interannual SST signal over the globe in order to identify seasons/areas where SST fluctuations are strong with a particular focus on the Southern Ocean.

As expected, the strong ENSO signal emerges as a SST standard-deviation maximum that extends from the coast of South America far into the west along the equator. Another important property of ENSO, well illustrated by Fig. 2, is the phase-locking of the SST variability to the annual cycle which manifests itself as a standard-deviation maximum (minimum) in December/January (April/May). This is related to the fact that many El Niño events start in boreal spring and peak in the eastern equatorial Pacific several months later in December-January. Variability of the SST fields is significantly weaker in the tropical Indian and Atlantic Oceans.

In the extra-tropical Northern Hemisphere, the SST interannual variability tends to be slightly larger during summer (around 0.8°-1.2°C). However, the patterns of variability are broadly similar in summer and winter. Numerous studies have shown that Northern Hemisphere SST variability in the cold season are generated primarily through the latent and sensible heat fluxes at the air-sea interface in association with large-scale atmospheric circulation anomalies linked to the North Pacific or North Atlantic (NAO) Oscillations (Cayan, 1992). The resulting SST patterns are still discernable during summer despite of the shallow mixed layer and may feedback onto the atmosphere in the next seasons through “the reemergence mechanism” (Zhang et al., 1998; Deser et al., 2003).

Another striking feature in Fig. 2 is the existence of relatively strong SST anomalies (around 0.4°-0.6°C) in the open Southern Ocean during austral summer (e.g. December-January and February-March) while Southern Hemisphere SST variability is rather weak during other seasons. This mid-latitude signal exists in the center of the three ocean basins and is distinct from the SST variability maxima observed in the tropical oceans.

Extra-tropical SST fluctuations in the Southern Hemisphere during austral summer are weaker than their northern counterparts during boreal summer. However, their origins are probably different since the northern SST signal is observed year-round and emerges from the western boundaries of the North Pacific and Atlantic Oceans. This suggests a strong contribution from Kuroshio and Gulf Stream fluctuations, respectively. On the other hand, the southern SST signal is strong only in (austral) summer and is obviously unrelated to upwelling processes or fluctuations of the western boundary currents (Huang and Shukla, 2006).

Venegas et al. (1997) have argued that the SST variability in the Southern Hemisphere is strongest during summer because of possible links with major tropical and Northern Hemisphere oscillations, which are strongest during boreal winter (ENSO, NAO, NPO, etc). However, the seasonal variations of SLP standard-deviations are not large in the Southern Hemisphere and the patterns are more or less the same for all seasons, excepted for a meridional translation due to the solar forcing (not shown). Interestingly, the depth of the surface mixed layer in the Southern Ocean mid-latitudes is the shallowest during austral summer, as a consequence of the weaker surface winds and the reduced vertical mixing at that time. Its climatological value is around 30-50 m in the three Southern Ocean basins during the December-March season (de Boyer Montegut et al., 2004). Since a simple anomaly of 10 W/m^2 in heat loss could lead to a local SST change of 0.5°C for a typical mixed layer depth of 50 m, this leads to the alternative hypothesis that SST variability maxima in the Southern mid-latitudes occur during austral summer, simply because wind-driven latent heat flux or shortwave radiation anomalies have more influence on SSTs at this time of the year due to the shallower summertime mixed layer (Suzuki et al., 2004). These two alternative hypotheses will be further verified in the next sections.

This originality of the Southern SST signal deserves further studies and the rest of this paper is devoted to a better understanding of the formation of these SST anomalies during austral

summer on one hand and to shed light on the reciprocal interactions between this southern SST signal and ENSO on the other hand.

3. SST variability in the Southern Hemisphere during austral summer

a. Uncoupled modes

As a first step for understanding dominant modes of SST variability in the Southern Hemisphere during the active austral summer season, bi-monthly SST anomalies during the 1979-2006 period have been decomposed using EOF analysis for the South Pacific, Atlantic and Indian Oceans, separately. The spatial domains of the EOF computations were chosen specifically to cover the areas of large standard deviations in the three southern oceans as illustrated in Fig. 2. More precisely, we define the South Pacific to be the area between 150°-290°E and 10°-50°S; the South Indian Ocean is the area between 25°-150°E and 10°-50°S; and finally the South Atlantic Ocean is between 50°W-25°E and 10°-50°S. The choice of 10°S as the northern boundary is somewhat arbitrary, however, translating this boundary to the South yields leading spatial patterns of SST variability that are similar and did not change the main results presented in the paper. The EOF analyses were also performed without combining the December-January (DJ) and February-March (FM) seasons in order to detect possible sub-seasonal differences in the space-time structure of the anomalous SST fields (Jin and Kirtman, 2009).

The leading EOF modes in each basin/season are well separated from the lower EOF modes in terms of explained variance, suggesting that these EOFs are robust and stable with respect to sampling errors (Table 1). Thus, only a discussion of the leading EOF modes of SST variability in the three southern ocean basins is given here.

The leading EOFs of DJ and FM SST anomalies in the South Pacific account for roughly comparable amounts of variance, 38% and 32% of the total area-weighted variance for their respective season, and are shown in Figures 3a and 3b. Moreover, these two EOFs are very similar and can be associated with the well-established ENSO-pattern: the positive SST anomaly in the eastern equatorial Pacific corresponds to an El Niño event and the surrounding cold and coherent anomaly on the southern side is a part of the well-known SST Pacific « horseshoe » pattern observed during the developing and mature phases of El Niño. There is

also a well-developed warm anomaly near 50°S, 120°W in both EOFs, which may be familiar to people working on the South Pacific (e.g. Kidson and Renwick, 2002; Kwok and Comiso, 2002). Apart from this similar spatial structure, the corresponding DJ and FM PC time series exhibit remarkably similar patterns of interannual variability (correlation of 0.92). All these features highlight the strong persistence of large-scale SST patterns in the South Pacific during austral summer.

Figures 3c and 3d show the leading SST EOF modes for the South Indian Ocean for the DJ and FM seasons. These modes describe 25% and 34% of the area-weighted variance for DJ and FM, respectively. During both seasons, a tilted subtropical dipole pattern oriented in the northeast-southwest direction emerges as the first mode of variability consistent with previous studies on South Indian Ocean variability (Behera and Yamagata, 2001; Fauchereau et al., 2003; Hermes and Reason, 2005; Huang and Shukla, 2007; Chiodi and Harrison, 2007). However, the observed SST dipole pattern is displaced poleward and the elongated negative region is more prominent and tilted during the FM season (Fig. 3d). Interestingly, the corresponding DJ and FM PC time series are also only moderately correlated together (0.55), suggesting only a modest temporal persistence despite of the similarity in spatial structure.

The first EOF modes in the South Atlantic for DJ and FM seasons explain about 30% of the total variance (Figs. 3e and 3f). EOF1 for the DJ season displays an out-of phase relationship between SST anomalies north and south of 25°-30°S and is very similar to spatial patterns derived by previous statistical studies in the South Atlantic region when all seasons are included in the EOF computations (e.g. Venegas et al., 1997; Sterl and Hazeleger, 2003; Huang and Shukla, 2006). At first sight, EOF1 of the Atlantic SSTs during FM looks very similar, but it can be seen that the SST dipole pattern is again shifted to the south and that the negative node is more prominent and shows a clear southeastward tilt across the basin during FM (Fig. 3f). Moreover, a strong cold anomaly is also observed along the western coast of Africa, confined to the coastal zone of Angola and Namibia in EOF1 during FM. This anomaly, reminiscent of the Benguela Niños/Niñas episodes in the southeast Atlantic Ocean (Florenchie et al., 2004), is absent in EOF1 during the DJ season. Finally, the DJ and FM PC time series are only weakly correlated (0.43) suggesting no persistence of SST anomalies from DJ to FM in the South Atlantic domain.

To look for possible links between SST anomalies in the South Indian, Atlantic and Pacific

Oceans, the correlation coefficients between the time series of the six discussed SST modes are calculated and displayed in Table 2. In DJ, the strong and significant correlations between the first PCs, derived independently for each ocean basin, suggest that the associated EOF modes can be regarded as the regional expression of a global-scale Southern Hemisphere mode of variability. This is confirmed by performing EOF analysis of DJ SST anomalies over the whole circumpolar ocean (Fig. 4a). The first EOF mode of SSTs on this larger domain reveals the same spatial structures as found above for the South Pacific, Indian and Atlantic Oceans separately.

Surprisingly, the connections between SST anomaly patterns in the South Pacific and the two other oceanic basins weaken considerably during the FM season (Table 2); in particular, the South Atlantic variability is largely independent of the variability in the South Pacific during FM (e.g. the correlation between the first PCs in each basin is -0.29). It is, however, worth pointing out that the leading modes of variability in the South Atlantic and Indian Oceans remain highly inter-related during FM (see Table 2). The high correlations between the leading EOFs in the South Atlantic and Indian Oceans, particularly during FM, suggest that, rather than thinking of these leading EOFs as different modes of SST variability, it may be more appropriate to think of them as a single mode of variability (Fauchereau et al., 2003; Hermes and Reason, 2005). This idea is again confirmed by performing EOF analysis on a combined South Atlantic and Indian domain during FM (Fig. 4b). As expected, the first EOF on this larger domain shows a quadrupole structure displaced poleward, exactly consistent with the previous EOF analyses restricted to each basin during FM. The robustness of this quadrupole structure was further tested by computing correlations between each center of the quadrupole and the global Southern Hemisphere SST anomalies during FM: each correlation map exhibits again the shifted subtropical dipole patterns in both the South Indian and Atlantic Oceans, and highly significant correlations with the other nodes of the quadrupole SST pattern (not shown).

On the other hand, performing an EOF analysis of FM SST anomalies on the whole circumpolar ocean gives a leading SST mode that is dominated by the variability in the South Pacific and with a spatial pattern exactly similar to the one observed during the DJ season, but with very low amplitude spatial loadings over the Indian and Atlantic basins (not shown). Hermes and Reason (2005) and, more recently, Morioka et al. (2009) have also highlighted the existence of significant differences in the position of the positive and negative poles

during subtropical dipole events in both the South Indian and Atlantic Oceans. However, the tight phase locking of these differences to the annual cycle was not observed before to our knowledge. Just why this particular quadrupole SST pattern exhibits only a weak persistence from DJ to FM, in addition to a poleward shift, is also a question of particular interest.

The origin of the circumpolar mode of SST variability during DJ and of the shifted quadrupole SST pattern over the South Atlantic and Indian Oceans during FM are further investigated in the next section.

b. Coupled modes

In this section, organized patterns of coupled ocean-atmosphere variability are identified using SVD analyses between SST and SLP fields (Figs. 5, 6 and 7). Considering the apparently significant phase locking of the SST anomalies to the annual cycle in the Southern Hemisphere, these SVD analyses are also conducted on a season-by-season basis as for the EOF analyses. The chosen SLP domain for the various SVD analyses have been extended to the South in order to take into account the possible influence of higher latitudes modes of atmospheric variability on the mid-latitudes SST fluctuations of the Southern Hemisphere (Hall and Visbeck, 2002). However, the SVD results are not sensitive to the particular domains used, both for the SLP and SST fields.

Table 3 presents summary statistics for the different SVD analyses, including the Squared Covariance Fraction (SCF) and the Normalized root-mean-square Covariance (NC) for the leading modes in the various SVD expansions, and the correlation coefficient (r) between the leading SV time series of the SLP and SST fields in each case. These statistics will be used here to investigate and compare the strength of the ocean-atmosphere coupling in each basin and season. Furthermore, the leading SVD modes explain by far the most SCF of the corresponding covariance matrices in each basin/season (Table 3). This explains our decision to include only these leading SVD modes in each basin/season in the following discussion.

The three leading SVD modes of the coupled SST and SLP variations in the South Pacific, Indian and Atlantic Oceans account, respectively, for 78%, 43% and 59% of the total square covariance for the DJ season and 61%, 45% and 53% for the FM season. The NC statistic and correlation coefficient r between the expansion coefficients of the SST and SLP SVD modes

are particularly strong for the Pacific Ocean during DJ, but they decreased during FM. On the other hand, these statistics are generally higher during FM than those observed during the preceding DJ season for the Indian and Atlantic Oceans. In other words, these statistics suggest a stronger ocean-atmosphere coupling during DJ for the Pacific Ocean, but during FM for the South Atlantic and Indian Oceans.

The leading SST patterns derived from these SVD analyses are not shown because they all closely resemble the respective SST EOF patterns illustrated in Fig. 3: their spatial structures are exactly similar and their expansion coefficient time series are correlated with the corresponding PCs at levels in excess of 0.77 and 0.97, for the DJ and FM seasons respectively. These correlations coefficients are particularly high for the South Pacific during the whole austral summer (e.g. greater than 0.99) and for the South Indian and Atlantic Oceans during FM (e.g. 0.99 and 0.97, respectively). This exact correspondence between the respective first SST EOF patterns on one side and the first SST SVD patterns on the other side may be taken as additional evidence of the physical meaning and robustness of the SST EOFs and of the relevance of the ocean-atmosphere coupling for explaining the observed SST patterns in the Southern Hemisphere during austral summer.

During the DJ season, all the leading SLP SVD modes in the three ocean basins of the Southern Hemisphere show a strong zonal symmetry with a phase reversal between high and mid-latitudes (Figs. 5ace). This pattern with a phase reversal between SLP anomalies in the Southern Hemisphere high and mid-latitudes is reminiscent of the SAM (e.g. Thomson and Wallace, 2000). In both the South Pacific and Indian Oceans, the signature of the Southern Oscillation with SLP anomalies of opposite polarity between Australia and the central and eastern tropical Pacific is also clearly discernible. On the other hand, the leading SLP SVD mode in the South Atlantic nearly vanishes in the tropical areas and the SLP signal is confined in the high and mid-latitudes of the South Atlantic (Fig. 5e).

Consistent with the high persistence of the leading SST anomalies pattern in the South Pacific from DJ and FM (Figs. 3ab) and the strong ocean-atmosphere coupling in that area during the whole austral summer illustrated in Table 3, the leading SLP SVD mode during FM closely resembles the leading SLP SVD mode during DJ in the South Pacific (compare Figs. 5a and 5b).

On the other hand, the leading SLP SVD modes in both the South Atlantic and Indian Oceans during FM are radically dissimilar to those observed during the previous DJ season (Figs. 5df). During FM, the leading modes of coupled SLP variability consist of a dipole zonally oriented in the South Indian Ocean and tilted in the northwest-southeast direction in the South Atlantic Ocean, with a very strong positive center of action around 45°S in both basins. As it is well-known, the SLP and wind fields over the South Atlantic and Indian Oceans are dominated by the subtropical anticyclones whose centers are located near 30°S, 5°W and 30°S, 90°E, respectively, during austral summer (Venegas et al., 1997; Behera and Yamagata, 2001). The positive centers of action in the leading SLP SVD patterns in the South Indian and Atlantic Oceans during FM, are located slightly southwestward of the center of the subtropical anticyclones in each basin. Hence these modes describe both a change in the location and the strength of these subtropical anticyclones. Furthermore, the spatial loadings over the tropical areas nearly vanish in the SLP SVD patterns of both the South Atlantic and Indian Oceans during FM season. This suggests that the modulation of the strength of the subtropical highs depicted by the leading SLP patterns in both the South Atlantic and Indian Oceans is relatively free from tropical influences to a first order.

Figures 6 and 7 show the time coefficients of the leading SST and SLP SVD modes in each basin and the Niño34 SST index for the DJ and FM seasons, respectively. The correlation coefficients at zero lag between the Niño34 SST index and the coefficient expansions time series of the SST and SLP SVD modes are also displayed in Figs. 6 and 7.

During the DJ season, all the SST and SLP SV time series are found to be highly and significantly correlated with the Niño34 SST index (Fig. 6). This suggests that ENSO has a highly discernible signal in the whole Southern mid-latitudes in addition to SAM during DJ season. This assertion is fully verified by performing a SVD analysis of DJ SST and SLP anomalies on the whole circumpolar ocean (Figs. 8ab). The SLP anomaly pattern obtained through this SVD analysis shows higher than normal SLP anomalies over the polar cap and below normal at mid-latitudes. The overall pattern is suggestive again of the SAM. This coupled SVD mode is also linked to the Southern Oscillation in the Tropics (Fig. 8b). Spatial distributions of SST and SLP anomalies in the Southern Hemisphere during ENSO and SAM episodes have also been obtained by computing correlation/regression maps between Niño34 SST index, or a SAM index, and the grid point SST and SLP anomalies (not shown). During the DJ season, the main centers of action displayed by these maps are analogous to those of

the leading SST EOF and SLP SVD modes depicted in Figs. 3, 5 and 8. Hence, the strong connection between the South Pacific, Atlantic and Indian Oceans described in the previous sections is likely a by-product of the fact that ENSO and SAM are the common denominator of the coupled patterns in each sector during DJ.

These ENSO and SAM forcings do not seem to persist during the FM season as far as the South Indian and Atlantic Oceans are concerned (Figs. 5df and 7): the SST and SLP SV time series for the Indian domain exhibit only a modest linear relationship with the Niño34 SST index at zero lag during FM (-0.39 and -0.34 for the SST and SLP SV1, respectively) while the corresponding time series in the South Atlantic seem to evolve in a completely independent fashion with respect to the Niño34 SST index (0.01 and 0.17, respectively). However, the possibility of a relationship between the South Atlantic and Indian leading modes of variability during FM (suggested by the high correlation between the FM PCs of the South Atlantic and Indian Oceans SSTs in Table 3 and Fig. 4b) is further supported by an SVD analysis of the SST and SLP fields during FM over a combined South Indian and Atlantic domain. The SST and SLP spatial patterns of the first SVD mode for this extended domain are displayed in Figs. 8c and 8d, respectively. These spatial patterns closely resemble those obtained from the SVD analyses in each basin separately. There is also a perfect similarity between the leading SST SVD and EOF patterns over the combined domain (compare Figs. 4b and 8c). This lends support to the existence of a connection between coupled variability in the South Atlantic and Indian Oceans during the late austral summer.

The processes involved in the air-sea interactions depicted by these coupled modes of variability of the Southern Hemisphere and the nature of the statistical links between these Southern Hemisphere fluctuations and ENSO is the focus of the next section.

4. Relationships with ENSO

a. Lead-lag relationships

To better assess the relationships between coupled variations in the Southern Hemisphere and ENSO, we begin this section by discussing the results of lead-lag correlation analyses

between the expansion coefficient time series of the leading EOF and SVD SST patterns described in the previous section and the Niño34 SST time series (Fig. 9).

Not surprisingly, the first leading SST SVD and EOF modes in each basin during the DJ season are highly correlated with the Niño34 SSTs over the period of study. SST PC1 and SV1 in the South Pacific, Indian and Atlantic Oceans have a contemporaneous correlation with the Niño34 index of 0.8/0.9, -0.6 and -0.7, respectively (Figs. 9ab). Overall, the highest correlations with ENSO are found when the PC or SV time series lag the Niño34 index by 0 to 6 months. Moreover, nearly no significant correlations are observed when the expansion coefficient time series lead the Niño34 time series by more than 4 months. One exception is the South Atlantic since the leading SST EOF mode for this basin during DJ exhibits modest, but significant, correlations with the Niño34 index at 10-18 months lead times (Fig. 9a). Hence, Figs. 9ab suggest that coupled patterns in the South Atlantic, Indian and Pacific regions during DJ are probably not very useful for extending the long-range predictability of ENSO.

Lagged correlations between the South Pacific leading SST EOF and SVD modes and Niño34 SSTs during FM suggest again a strong dependence with ENSO in the previous boreal fall and winter (Figs. 9cd). On the other hand, the highest correlations with the SST SVD and EOF modes over the South Atlantic and Indian Oceans during FM are found when the SV and PC time series lead the Niño34 SST index by 4-14 months. Although we might expect some quasi-cyclic behavior, the correlations for Niño34 SST index preceding SST SV1 and PC1 in both the South Atlantic and Indian Oceans (or the combined South Atlantic-Indian domain) were modest and generally not significant excepted for the South Indian Ocean. This implies that the expansion coefficient time series in both the South Atlantic and Indian Oceans are not residual patterns from a previous ENSO event with the opposite polarity during the preceding boreal winter. Interestingly, if we move 10° to the South the northern boundary of the Indian Ocean domain, the leading EOF is again reminiscent of the subtropical SST dipole pattern, but the relationship between this SST mode and ENSO during the preceding boreal fall and winter weakened considerably while this SST mode is again a highly significant precursor of ENSO at 4 to 14 months lead-times. Paraphrasing, the key regions for ENSO long-range predictability are in the extra-tropics of the Southern Hemisphere, not in the Tropics.

A difference should be made, however, between the correlations obtained with the Indian and Atlantic modes, respectively: the linear relationships with the South Atlantic Ocean are particularly strong at 2-4 months lead time (e.g. during boreal spring) and stay roughly constant afterward, while the correlations with the South Indian Ocean increase steadily and gain progressively high statistical significance from 4 to 14 months lead times. Hence, the potential "forcing" from the South Indian and Atlantic Oceans seems to act with different timings, in boreal spring and early summer for the Atlantic Ocean on one hand, and later, in summer and fall, for the Indian Ocean on the other hand.

Interestingly, from 4 to 14 months lead times, the best results are always obtained with the expansions coefficients of the leading modes of the combined South Atlantic-Indian domain, suggesting that both oceans may contribute to the long-range predictability of ENSO. Figure 10 displays the DJ Niño34 SST anomalies and the expansion coefficients of the first EOF and SVD modes of the SST and SLP fields over the South Indian-Atlantic domain during FM, ten months before. Overall, they track each other closely corroborating what we inferred from Fig. 9. With a few exceptions (e.g. the 2000-2004 sub-period), each positive (negative) peak of the Niño34 SST index is preceded by a positive (negative) peak in the expansion coefficient time series of the leading SST and SLP modes for the South Atlantic-Indian domain ten months before (e.g. before El Niño/La Niña onset). The significance of this relationship can also be illustrated by noting that all the major recent El Niño events have been preceded by blocking events in the South Indian and/or Atlantic Oceans during the late austral summer preceding the onset of these events (see also Figs. 7bc). Furthermore, the amplitude of the expansion coefficients of the EOF and SVD modes gives an amazingly exact prediction of the Niño34 interannual SST anomalies during the peak phase of the El Niño/La Niña events (Fig. 10). This is particularly true for the two strongest El Niño events ever recorded in the last century (e.g. 1982-83 and 1997-98) when the signals in both the South Atlantic and Indian Oceans were strong and in phase during FM of 1982 and 1997 before the onset of El Niño (see Figs. 7 and 10).

In view of these lead-lag correlations, there is scope for further investigations of the persistence of the subtropical SST dipole patterns over the South Indian and Atlantic Oceans. Of particular interest are the questions of whether these dominant patterns of SST anomalies persist from austral summer to boreal summer and whether they undergo a systematic evolution from season to season with a propagation of SST anomalies into the deep tropics

after the peak phase of the subtropical dipole events. It would seem that it is a necessary condition for accepting the hypothesis that mid-latitudes coupled variability in the South Atlantic and Indian Oceans may substantially influence the coupling over the equatorial Pacific in the following seasons, i.e. during the onset and development phases of ENSO events.

b. Life cycle of subtropical dipole events in the Southern Hemisphere

To address these questions, we have computed global SST regression maps upon the time series of the respective normalized expansion coefficients of the leading FM SST EOFs in both the South Atlantic and Indian Oceans (Fig. 11).

The regression maps show that the SST dipole patterns that are observed in the South Atlantic and Indian Oceans during FM are largely driven by SST changes that occur one to two seasons before in each oceanic basin. These SST changes are characterized by abrupt warming and cooling, which together cover nearly all the Atlantic and Indian basins South of the equator. Moreover, the cooling and warming trends tend to happen simultaneously in a specific basin and SST dipole-like variability in the South Atlantic and Indian Oceans are significantly correlated to each other. The observation of these abrupt summertime SST tendencies roughly collocated with the warm and cold poles of the dipole patterns in FM is consistent with the hypothesis that these anomalies form in austral summer because the ocean mixed layer depth is shallow then, making SST highly sensitive to surface heat flux anomalies (Suzuki et al., 2004).

The regression maps also support the hypothesis of a strong persistence of SST anomalies in both the Indian and Atlantic Oceans after the peak phase of the subtropical dipole events. The persistence is particularly high for the northeast (Indian) and north (Atlantic) poles of the subtropical SST dipole patterns. Furthermore, there is a clear northward propagation of the negative SST anomalies in the Atlantic Ocean from DJ to the boreal summer while such propagation is less obvious in the Indian Ocean.

Interestingly, there are also important differences over the tropical Pacific between the two regressed SST patterns: first the subtropical dipole events in the Indian Ocean are partly associated with a La Niña state in the equatorial Pacific during the previous boreal winter

(however, note that with an Indian domain restricted to the South of 20°S, the relationship weakens considerably) while this association does not hold for the South Atlantic Ocean; second, the subtropical dipole events in the South Atlantic lead to warm SST anomalies over nearly the whole equatorial Pacific from the date line to the east coast of Peru just after the peak phase of the event (e.g. April-May) and these anomalies are further amplified during the following months. By contrast, the subtropical dipole events in the Indian Ocean lead to warm anomalies over the equatorial eastern Pacific two months later, but they have a closer association with the concurrent cold SST anomalies over the western Pacific. They lead significantly the development of the southern branch of the traditional SST horseshoe pattern in the South Pacific. Consistent with Terray and Dominiak (2005), there is also a clear suggestion of a propagation of the cold SST anomalies from the Indian Ocean into the South Pacific during boreal spring.

In order to unravel processes leading to these SST changes, the temporal evolution of 850-hPa wind, SLP and OLR bi-monthly anomalies is shown in Figs. 12 and 13 from DJ to August-September (AS) seasons. Moreover, to check whether surface fluxes drive the SST anomalies of interest here, surface wind, latent heat flux and net shortwave radiation regression maps from DJ to April-May (AM) are also calculated and displayed in Figures 14 and 15. The evolution of anomalies associated with the strong anticyclone episodes in the South Atlantic and Indian Oceans displays distinct stages as described below.

1) Late boreal winter to spring

From DJ to FM, the 850-hPa wind and SLP anomalies show that the strengthening and displacement toward the southwest of the subtropical anticyclones are accompanied by stronger-than-normal southeasterly trade winds and weaker-than-normal westerlies in a band between 30°-40°S in the western part of both the Atlantic and Indian Oceans. The relationship between the wind and SST anomalies is direct and local: the northeasterlies to the west, and the southeasterlies to the northeast of the anomalous SLP center in each basin are collocated with warm and cold SST anomalies, respectively. Both the South Atlantic and Indian regression maps provide additional evidence that strong anticyclone episodes tend to happen simultaneously in both basins in some years. However, a closer inspection of the SLP and wind regression patterns reveals that the anticyclone pulses in the South Atlantic lead the

corresponding events in the South Indian Ocean by one or two months, a finding consistent with the results of Hermes and Reason (2005).

Consistent also with previous studies (Venegas et al., 1997; Behera and Yamagata, 2001; Sterl and Hazeleger, 2003; Hermes and Reason, 2005), the latent heat flux regression maps, shown in Fig. 14, suggest that the SST anomalies are partly driven by the surface latent heat fluxes. Wind speed and specific humidity regression maps computed from the OAFLUX products (not shown) demonstrate that this latent heat flux variability is linked to both wind speed variability (e.g. Suzuki et al., 2004) and near surface humidity variability associated with meridional advection of water vapor (e.g. Chiodi and Harrison, 2007).

While the primacy has been made for latent heat flux as the main contributor to the growth and decay of dipole events in the two basins (Sterl and Hazeleger, 2003; Suzuki et al., 2004; Hermes and Reason, 2005; Chiodi and Harrison, 2007), net shortwave radiation and mixed layer depth regression maps suggest that the summertime subtropical dipole variability in both the South Atlantic and Indian Oceans are in fact driven by a variety of geographical dependent processes, including cloudiness variations and wind-induced vertical mixing. The mixed layer deepens significantly in the eastern Indian and Atlantic Oceans during the strong anticyclone episodes, probably through wind-induced ocean mixing, and may also contribute to the creation of the SST dipole patterns in both oceans (not shown). In agreement with the results of Hermes and Reason (2005), negative net shortwave radiation anomalies occur also in association with below normal SST in the eastern South Atlantic Ocean during DJ and the eastern Indian Ocean during FM (Fig. 15). As described above, these negative net shortwave radiation anomalies occur in conjunction with southeasterly winds and enhanced cold advection (Fig. 12). In the southwestern Atlantic and Indian Oceans, the relationship between the net shortwave radiation and surface wind anomalies during austral summer is less clear, but suggests also that northerly wind anomalies and tropical warm advection during the blocking events are associated with increased shortwave radiation anomalies over the southwestern Indian or Atlantic Oceans.

Moreover, a positive feedback between SST and marine cloudiness is possible over the eastern subtropics of both the Indian and Atlantic Oceans: lower SST induced by the stronger-than normal southeasterly trade winds favors enhanced marine stratiform cloudiness in the southeastern part of each ocean by modifying the structure of the atmospheric boundary layer

and enhanced cloudiness cools further the ocean mixed layer. Such a positive feedback could substantially lengthen the persistence time of the northern node of the Atlantic and Indian subtropical SST dipole patterns as illustrated in Fig. 11.

Finally, the atmospheric teleconnections associated with the development of the strong anticyclone episodes in the South Atlantic and Indian Oceans are significantly different. The DJ SLP and 850-hPa wind regression maps for the leading SST EOF mode over the South Atlantic emphasized a NAO link (Venegas et al., 1997). On the other hand, the corresponding maps for the South Indian Ocean feature a significant Southern Oscillation pattern in the Indo-Pacific region. Specifically, the anomalous cyclonic wind anomalies over the equatorial and tropical South Indian Ocean may be interpreted as a Rossby-type response to enhanced condensational heating over the maritime continent and the western equatorial Pacific (Lau and Nath, 2000, 2003). In turn, these circulation anomalies enhance the seasonal flows over the equatorial and South subtropical Indian Ocean and may be responsible for the appearance of the initial cold SST anomalies over the eastern Indian Ocean due to the enhanced upward surface latent heat flux in relation to increased surface wind speed in both areas and reduced incoming shortwave radiation associated with enhanced convection in the eastern part of the Indian basin (Fig. 13a). These differences in teleconnection patterns may reflect that strong anticyclone episodes in the South Atlantic and Indian Oceans have a different physical origin despite the strong statistical links between SST dipole patterns in the two basins.

2) *Boreal spring to summer*

During FM to AM in the Atlantic Ocean and AM in the Indian Ocean, the SLP and 850-hPa wind regression maps are suggestive of an immediate adjustment of the atmosphere to the anomalous SST gradients induced by the strong anticyclone episodes: a northward displacement of the positive SLP anomalies is clearly seen in each basin (Fig. 12). In both the Indian and Atlantic sectors, these SLP anomalies are lying now over the cold SST anomalies induced by the trade winds and cloudiness fluctuations observed in DJ and FM. Moreover, an anomalous cyclonic circulation coincides with the warm SST anomalies over the southwest Indian Ocean, just west of Madagascar during AM. All these evidences support the existence of an ocean-to-atmosphere forcing in both the Atlantic and Indian Oceans during boreal spring.

Further support for this hypothesis comes from the OLR, latent heat flux and surface wind regression maps (Figs. 13 and 14). Over the Indian Ocean, the OLR anomalies display an obvious north-south contrast, just south of the equator, which suggests that the northward migration of the Inter-Tropical Convergence Zone (ITCZ) is considerably delayed or significantly weakened during AM. In deed, the observed wind, SLP and OLR anomalies are of the right polarity to be interpreted as a linear response to heating resulting from the anomalous SST gradient in the South Indian Ocean (Lindzen and Nigam, 1987).

This significant south-north anomalous SLP gradient over the South Indian Ocean during AM produces a weakening of the climatological easterly wind around 15-20°S, but a strengthening of both the easterly wind to the north and the seasonal southeasterly wind between Java-Sumatra and Australia (Fig. 14a). The weaker-than-normal wind in the south tropical Indian Ocean results in reduced upward latent heat fluxes while the stronger-than-normal winds to the north and off the Java-Sumatra coast produce the opposite effect due to increases in surface wind speed (Fig. 14a). On the other hand, the large reduction of convection between the equator and 20°S in the central and eastern Indian Ocean implies less cloudiness over the South tropical Indian Ocean during AM as suggested by the positive and significant net shortwave radiation anomalies between 5° and 20°S over the south Indian Ocean (Fig. 15a). These features may explain why the subtropical dipole induced SST anomalies are destroyed in the western Indian Ocean, and why the cold SST anomalies tend to persist over the eastern Indian Ocean from FM to June-July (JJ) (see Fig. 11a). Furthermore, the stronger-than-normal trade-winds off the Java-Sumatra coast from AM to JJ (Fig. 14a) may also trigger other oceanic dynamic processes (e.g. upwelling and wind-thermocline-SST feedback) which may further sustain the cold anomalies over the eastern Indian Ocean through the boreal spring, summer and fall, as demonstrated by the coupled model study of Terray et al. (2007).

From FM to AM, the strong negative SST anomalies associated with the leading SST EOF mode in the South Atlantic Ocean persist just south of the equator, while SST anomalies are weakly positive and insignificant over the North Atlantic Ocean (Fig. 11b). As such, a cross-equatorial SST gradient develops over the tropical Atlantic Ocean from FM to AM. During FM, surface wind anomalies display an obvious north-south contrast consistent with this cross-equatorial SST gradient, with southeasterly wind anomalies over the South and equatorial Atlantic Ocean and southwesterly wind over the North Atlantic Ocean (Fig. 14b). From AM, the northward displacement of the high pressure anomalies is accompanied by a

relaxation of the stronger-than-normal trade winds in the subtropical areas, but stronger southeasterlies are still observed south of the equator, particularly in the west, as are the southerlies or southwesterlies just north of the equator (Fig. 14b). In association with these wind anomalies, latent heat flux anomalies show also a similar contrast with enhanced upward latent heat flux south of the equator and reduced upward latent heat flux north of the equator. In other words, it seems that subtropical dipole events in the South Atlantic Ocean are able to trigger the so-called WES feedback over the tropical Atlantic Ocean during boreal spring (Chang et al., 2006).

From FM to JJ, OLR and net shortwave radiation anomalies over the tropical Atlantic Ocean are symmetric about the equator with large and positive anomalies over the equator and negative anomalies between 10-20°S in each hemisphere (Figs. 13b and 15b). The large south wind anomalies in the trades observed from DJ to AM over the equatorial Atlantic Ocean associated with the leading FM Atlantic SST EOF mode are consistent with a northward migration of the ITCZ during the boreal spring and early summer. At the same time, significant negative OLR and net shortwave radiation anomalies are observed over the latitudinal band centered around 20-30°S, just south of the cooling of the ocean induced by the strong anticyclone pulse one season before. In deed, all these local relationships suggest again that the formation of the OLR and surface wind anomalies over the tropical Atlantic Ocean are related to the cross-equatorial and south subtropical SST gradients. Moreover, the earlier appearance of the cold SST anomalies just south of the equator than the wind and OLR anomalies over the tropical Atlantic Ocean during spring is consistent with this hypothesis. From AM to JJ, negative SST anomalies extend to the north of the equator in the eastern part of the Atlantic basin. Accordingly, the wind, latent heat flux and OLR anomalies weaken (Figs. 13b and 14b). This suggests the end of the WES feedback over the tropical Atlantic Ocean.

3) *Relationships with Pacific variability*

The ITCZ is normally close to the equator over both the Indian and Atlantic Oceans in AM. Interestingly, the spatial patterns of OLR, SLP and wind anomalies over the tropical Indian and Atlantic Oceans induced by the strong subtropical anticyclone episodes during boreal spring oppose to these seasonal changes and contribute to the weakening of the ITCZ over both the equatorial Atlantic and Indian Oceans. This, in turn, seems to induce significant and

persistent negative OLR and surface westerly wind anomalies over the western and central equatorial Pacific from the boreal winter to the next summer (Figs. 13 and 14). Now, these wind anomalies may be important for ENSO variability because the anomalous westerlies over the western Pacific may generate oceanic-downwelling Kelvin waves which propagate eastward and may be responsible for the El Niño onset observed a few months after the occurrence of the positive dipole events in the South Atlantic and Indian Oceans, respectively (see Figs. 9 and 11). During JJ, the warm SST and westerly wind anomalies are observed over much the tropical Pacific in both the South Indian and Atlantic regression maps (Fig. 14), suggesting that the local Bjerknes feedback is already strong enough to support the rapid growth of El Niño in the two cases. In summary, the western Pacific wind anomaly is a key variable in the connection between ENSO and the subtropical dipole events in the South Atlantic and Indian Oceans.

To examine in more details the atmospheric dynamics of interaction between the El Niño onset and the subtropical dipole events in the South Atlantic and Indian Oceans, 200-hPa velocity potential, streamfunction and upper-level (400 and 200-hPa) temperature correlation patterns and their related upper-level wind anomalies during AM are shown in Fig. 16. For simplicity, we just show the correlation/regression maps derived from the combined South Atlantic and Indian SST leading EOF since the associated expansion coefficient time series gives the best long-range ENSO prediction (see Figs. 9 and 10a). To further diagnose the temporal relationships between the western Pacific westerly wind and OLR anomalies and the subtropical Atlantic and Indian dipole modes, potential temperature longitude-height sections along the equator are also displayed in Fig. 17.

In the velocity potential correlation map (Fig. 16c), the negative (positive) correlations correspond to the divergent (convergent) response associated with enhanced convection (subsidence). Thus, the large seesaw between the Pacific and the two other oceans in the velocity potential correlation map during AM lends weight to the idea that the significant westerly wind anomalies which occur over the western Pacific before the onset of many previous El Niño events were significantly controlled by large-scale ascendance and deep convection over the western equatorial Pacific remotely forced by strong large-scale descending motion over the two other tropical oceans. Observational studies have established that a high absolute SST is necessary for deep convection to occur (Graham and Barnett, 1987). However, even when SSTs are high, as in the western Pacific warm pool, convection

may be suppressed (or enhanced) by other factors such as upper level subsidence (ascendance) generated by remote forcing (Lau et al., 1997).

Following this way of reasoning, it is interesting to observe that the enhanced convection over the western Pacific is associated with significant cold anomalies at upper levels which can be traced back to variations in the tropical convection patterns other the Indian and Atlantic Oceans (Figs. 16ab). Both the 400 and 200-hPa temperature correlation maps show a significant cold temperature anomaly extending eastward along the equator from the Atlantic and Indian Oceans to the western equatorial Pacific. Moreover, over both the Atlantic and Indian Oceans, there are two cold poles away from and straddling the equator at 400-hPa. All these features are reminiscent of a Kelvin wave response (Gill, 1980). The 200-hPa wind regression pattern also shows the existence of strong westerly (easterly) anomalies over the eastern (western) equatorial Pacific suggesting a strong interaction between the three tropical basins during boreal spring. Because the tropical atmosphere cannot support large temperature gradients, the anomalous cooling over the Atlantic and Indian Oceans induced by the weakening of the equatorial ITCZ in these regions spread rapidly to the western Pacific through planetary waves in the upper atmosphere. In deed, the 400 and 200-hPa temperature correlation patterns suggest that the enhancement process for the local convection and westerly surface wind events over the western Pacific may be triggered by this huge temperature response in the upper atmosphere remotely forced by the large-scale subsidence over the Atlantic and Indian Oceans. The resulting negative temperature anomalies at upper levels may lead to a destabilization of the atmospheric column over the remote western Pacific, a hypothesis largely supported by the potential temperature equatorial vertical cross-sections displayed in Fig. 17.

The potential temperature equatorial vertical cross-sections show significant positive temperature anomalies over the western Pacific at low levels first in AM for the Atlantic mode and JJ for the Indian mode (Fig. 17). This warming of the lower levels of the atmosphere is certainly related to the enhanced convection over the western equatorial Pacific (Fig. 13). However, the most interesting feature here is that this significant warming of the low and mid-troposphere is collocated with significant cold temperature at upper levels in both regression maps. In other words, this suggests again that the cold temperature advection at upper levels sets the stage for deep convection by destabilizing the vertical structure of the atmosphere (e.g. due to the increased vertical temperature gradient) and by decreasing the

value of surface boundary layer moisture required for the convection to occur over the western equatorial Pacific (Fig. 13). After this first triggering stage, warming develops progressively over the central Pacific at both lower and upper levels of the troposphere due to the eastward shift of the convection center and the latent heat release at upper levels, respectively.

The vertical cross-sections of potential temperature anomalies along the equator illustrate again that the Indian and Atlantic Oceans have a distinct signature over the western Pacific and play complementary roles in forcing ENSO. The Atlantic Ocean seems to play a dominant role during the El Niño onset (e g. FM to JJ) while the Indian Ocean contributes to a relatively fast transition from La Niña to El Niño and is the dominant player after the El Niño onset phase.

Finally, significant circulation centers are found over the tropical Indian, Pacific and Atlantic Oceans in the 200-hPa streamfunction correlation pattern during AM (Fig. 16d). The correlation pattern has the expected anticyclone pairs straddling the equator in the equatorial western Pacific, near the area of enhanced convection and upper-level divergence at 200-hPa as indicated by the OLR and velocity potential patterns (e.g., Gill, 1980). However, significant cyclonic circulation centers are also found in both the western Indian and Atlantic Oceans lying to the west of regions of reduced convection and strong upper-level convergence at 200-hPa of almost equal intensity as those found in the Pacific. The negative OLR forcing over the equatorial western Pacific which corresponds to enhanced convection and positive divergence, seems to act as a Rossby wave source and a well-organized wave-train structure prevails over the Southern Hemisphere mid-latitudes with alternate negative and positive streamfunction anomalies emanating from the western Pacific. Zonal upper level winds in the South Pacific near the date line are strengthened at 20°-30°S and also appreciably weakened just south of New Zealand (Fig. 16b), suggesting a northward displacement of the subtropical upper-level jet in the South Pacific (Terray and Dominiak, 2005). Correspondingly, an elongated zone of negative SLP anomalies prevails over the subtropical South Pacific during AM (Fig. 12). In deed, quasi-stationary circulation anomalies resulting from the Rossby wave response to the western Pacific heat source are observed at both the surface and upper levels in the South Pacific, highlighting a barotropic structure (Figs. 12 and 16). The significant negative SLP anomalies prevailing over the southeast Pacific sector suggest that the South Pacific Subtropical High (SPSH) is slightly displaced

southward from its normal position (Fig. 12). In turn, this southward displacement of the SPSH will also weaken the southeasterlies at the northern edge of this high, resulting in a relaxation of the South Pacific trade-wind system which may also further amplify the development of ENSO (e.g. Van Loon, 1984; Toniazzo, 2009).

5. Conclusions and discussions

The present study suggests that extra-tropical atmospheric forcing of ENSO may be more important than previously thought. A recent study by Vimont et al. (2009) dealing with the NPO and its influence on the tropical Pacific supports also this hypothesis. More precisely, our analysis of observational estimates during recent decades shows a southern extra-tropical atmospheric influence on tropical processes and the development of persistent zonal wind anomalies over the western equatorial Pacific.

Active SST fluctuations over the open ocean of the Southern Hemisphere are strongly phase-locked to the austral summer season. Several studies have suggested that this seasonal phase-locking of the SST anomalies in the Southern Hemisphere may be attributed to the shallowing of the mixed layer during summertime in such way that the latent heat flux and shortwave radiation anomalies influence the SST anomalies more efficiently during this season (Suzuki et al., 2004; Huang and Shukla, 2006, 2007; Morioka et al., 2009). Another possibility, not exclusive of the previous one, for explaining this intriguing result is the observation that the ocean/atmosphere coupling is stronger during summertime in the Southern Hemisphere because of possible links with major climatic oscillations observed in the Tropics (ENSO) or the Northern Hemisphere (NAO and NPO), which are strongest during boreal winter (Venegas et al., 1997). Our analysis suggests that this later factor plays an important role during the early austral summer (DJ) while the former factor is dominant during the late austral summer (FM).

EOF and SVD analyses reveal significant differences in the space-time structure of SST and SLP variability in the mid-latitudes of the Southern Hemisphere during the early (DJ) and late (FM) austral summer as well as distinct lead-lag relationships with ENSO. For the early austral summer period, the leading SLP and SST EOF or SVD modes in the three ocean basins of the Southern Hemisphere are significantly related to each other and may be considered as the regional components of a global circumpolar mode of coupled ocean-

atmosphere variability. Further statistical analyses show that this circumpolar mode of coupled variability is primarily driven by SAM and ENSO (Karoly, 1989; Mo, 2000). However, further work along the lines of L'Heureux and Thomson (2006) will be necessary to disentangle the respective influence of ENSO and the annular mode in the Southern Hemisphere mid-latitudes during DJ. Consistent with previous studies on the Southern Hemisphere interannual climate variability, our analysis show also that these large-scale extra-tropical SST variations observed during the first part of the austral summer in the Southern Hemisphere are unlikely to make a significant contribution to ENSO long-range predictability (e.g. Kidson and Renwick, 2002).

Surprisingly, these ENSO and SAM forcings do not seem to persist during the FM season as far as the South Indian and Atlantic Oceans are concerned. In a recent study, Jin and Kirtman (2009) show that the ENSO-related Rossby wave train in the Southern Hemisphere is strongest one season prior to the ENSO mature season (e.g. DJF) and that this Southern Hemisphere response to ENSO weakens abruptly in the peak phase of ENSO, during the late austral summer. Based on some numerical experiments, these authors argue that the ENSO response in the Southern Hemisphere significantly depends on seasonality. This hypothesis may explain why the South Atlantic and Indian Oceans variability is largely decoupled from the South Pacific and ENSO during FM. Our observational analysis confirm that the FM leading coupled SST and SLP modes in the South Indian and Atlantic Oceans which are characterized by a subtropical SST dipole pattern and a strengthening (or weakening) of the subtropical anticyclones seem less subject to interannual variability forced by the ENSO cycle in the Tropics or the SAM in the southern high latitudes. Hence, these coupled modes during the late austral summer better reflect the occurrence of blocking events and the intrinsic evolution of the coupled climate system in the southern mid-latitudes on interannual time scales. It has been suggested that this type of SST anomaly pattern may also be initiated by the oceanic response to mid-latitude atmospheric fluctuations over the Atlantic and Indian Oceans (Sterl and Hazeleger, 2003; Chiodi and Harrison, 2007). Moreover, our analysis confirms that, in some years but not all, these subtropical events tend to happen simultaneously in both the Atlantic and Indian Oceans (Fauchereau et al., 2003; Hermes and Reason, 2005).

So far, recent interest in determining the cause of these subtropical SST anomalies is mainly due to the possible linkages between these modes and austral summer rainfall in South Africa,

Australia and America (England et al., 2006, Morioka et al., 2009). On the other hand, preliminary results presented here suggest that these Southern Hemisphere extra-tropical modes of variability may exert a significant influence on ENSO and the tropical climate after the 1976-77 climate shift. The significance of this relationship can be illustrated by noting that all the recent major El Niño events have been preceded by blocking episodes in the South Indian and/or Atlantic Oceans during the austral summer preceding the onset of these events. Moreover, our observational results suggest that the co-occurrence of the subtropical dipole events over the South Atlantic and Indian Oceans, as in the boreal winter of 1981-82 and 1996-97, leads to a fast El Niño onset and tends to be accompanied by a very strong event in the next boreal winter.

We found that westerly wind anomalies over the western equatorial Pacific involved in El Niño onsets may be induced by the large-scale motion arising from differential heating of the atmosphere between the Pacific warm pool and the tropical Indian and Atlantic Oceans during late boreal winter and spring and not only the local SST (Lau et al., 1997). More precisely, the strength of convection over the western Pacific is partly determined by the vertical instability of the atmospheric column resulting from cold air advection from the surrounding environment at upper levels. Furthermore, our results suggest that the enhancement process for the local convection over the western Pacific may be triggered by a "cold Kelvin" wave at middle and upper levels in the atmosphere remotely forced by the large-scale subsidence over the Atlantic and Indian Oceans. This local increase of deep convection may promote persistent wind anomalies, energetic but isolated wind bursts or even local enhancement of an active phase of the tropical intraseasonal oscillation over the western Pacific sector (Lau et Chan, 1998; Moore and Kleeman, 1999). These westerly zonal wind anomalies at a variety of time scales can induce eastward-propagating equatorial downwelling Kelvin waves along the thermocline in the Pacific which lead to a significant surface warming in the eastern and central equatorial Pacific, two to three months later (Chang et al., 2006). This initial warming may then trigger the Bjerknes feedback responsible for the El Niño growth. In turn, the large-scale subsidence over both the tropical Indian and Atlantic Oceans are linked to cold local SST anomalies and anomalous subtropical SST gradients, mainly generated by subtropical dipole events one or two seasons before and sustained by a variety of coupled feedbacks in both the Indian and Atlantic Oceans. By this sequence of events supported by our regression analyses, we propose that subtropical dipole variability in both the Indian and Atlantic Oceans may serve as a trigger for ENSO during recent decades.

In contrast to the pessimism view on the long-range predictability of ENSO in relation with the role of stochastic forcing (Moore and Kleeman, 1999; Flugel et al., 2004; Chang et al., 2006), the important point highlighted by our analysis is that the knowledge of the large-scale background atmospheric state controlling the evolution of the zonal wind anomalies after the specific triggering process seems to play a key-role for the developing El Niño. In other words, given the appropriate large-scale SST structure and background atmospheric state, the uncertainty regarding the precise date of occurrence and characteristics of the westerly wind anomalies may not matter significantly to the large-scale ENSO dynamics (Tziperman and Yu, 2007).

A few studies have addressed the existence of persistent atmospheric circulation anomalies and the occurrence of blocking events in the Southern Hemisphere (Trenberth and Mo, 1985; Renwick, 2005). These studies have revealed an important blocking region over the southeast Pacific, which is strongly linked to ENSO. This blocking region is collocated with the main center of action in our leading SLP SVD mode over the South Pacific during austral summertime. In addition, blocking is sometimes observed to occur simultaneously in the New Zealand region, the South Atlantic, and the Southern Indian Ocean, in a global and zonal wavenumber-3 (ZW3) pattern. A notable feature of this ZW3 pattern is a marked upward trend in its activity in both the ECMWF and NCEP reanalyses (Renwick, 2005). The upward trend in ZW3 occurrence during recent decades may be partly an artifact due to the introduction into the reanalyses of satellite information in the late 1970s, but parts of this signal seems also robust (Gillet and Thomson, 2003). Interestingly, this ZW3 pattern bears a strong resemblance to our leading SLP SVD mode over the combined South Atlantic and Indian domain during FM. The relationships between the apparent upward trend in ZW3 occurrence and the Southern Hemisphere forcing of ENSO described here merit clearly further investigations in the future. It is hoped that such studies will offer new insights into the decadal variability of long-range predictability of ENSO.

Alternatively, it is conceivable that the sudden warming of both the Atlantic and Indian Oceans observed during recent decades have played an important role in the tropical-extra-tropical interactions described here by changing the background SST state in the subtropics, as already suggested by Terray and Dominiak (2005). Understanding the detailed physical processes and identifying causality between the equatorial Pacific and off-equatorial modes of

variability in the South Indian and Atlantic Oceans is obviously required to confirm the role of subtropical Indian and Atlantic dipole-like variability in the onset and development of ENSO events in the context of the global warming due to the short record used here. Such studies may also probably give new insights on the future of ENSO and its long-range predictability.

To this end, it will be of interest to determine whether coupled models are capable of simulating the Southern Hemisphere coupled interactions and their impact on ENSO described in this paper.

Acknowledgments: Financial support from the Indo-French CEFIPRA project (N° 3907/1), the French program "Les Enveloppes Fluides et l'Environnement » (LEFE: project MISSTERRE) and the ENSEMBLES European project (contract GOCE-CT-2003-505539) are acknowledged. The Hadley SLP and SST, NCAR/NCEP reanalysis and NOAA OLR datasets were provided by the NOAA/OAR/ESRL PSD, Boulder, Colorado, USA, from their Web site at URL: http://www.cdc.noaa.gov/. The OAFLUX products are obtained from the Woods Hole Oceanographic Institute through ftp://ftp.whoi.edu/pub/science/oaflux/data. Graphics have been prepared using the SAXO package of Sébastien Masson.

References

Alexander, M. A., I. Bladé, M. Newman, J. R. Lanzante, N.-C. Lau, and J. D. Scott (2002) The atmospheric bridge: The influence of ENSO teleconnections on air–sea interaction over the global oceans. *J. Climate,* **15,** 2205–2231.

Allan, R., and T. Ansell (2006) A New Globally Complete Monthly Historical Gridded Mean Sea Level Pressure Dataset (HadSLP2): 1850-2004. *J. Climate*, **19**, 5816-5842.

Anderson, B. T. (2003) Tropical Pacific sea-surface temperatures and preceding sea level pressure anomalies in the subtropical North Pacific. *J. Geophys. Res.*, **108**, 4732, doi:10.1029/2003JD003805.

Annamalai, H., S.-P. Xie, J. P. McCreary, and R. Murtugudde (2005) Impact of Indian Ocean sea surface temperature on developing El Niño. *J. Climate*, **18,** 302-319.

Behera, S.K., and T. Yamagata (2001) Subtropical SST dipole events in the southern Indian Ocean. *Geophys. Res. Lett*., **28**, 327-330.

Bretherton, C., Smith, C. and J. Wallace (1992) An intercomparison of methods for finding coupled patterns in climate data. *J. Climate*, **5**, 541-560.

Carleton, A.M. (2003) Atmospheric teleconnections involving the Southern Ocean. *J. Geophys. Res.*, **108**, NO. C4, 8080, doi:10.1029/2000JC000379.

Carril, A.F., and A. Navarra (2001) Low-frequency Variability of the Antarctic Circumpolar Wave. *Geophys. Res. Lett.*, **28**, 4623-4626.

Cayan, D. R. (1992) Latent and sensible heat flux anomalies over the northern oceans: The connection to monthly atmospheric circulation. *J. Climate,* **5**, 354–369.

Chang, P., and Coauthors (2006) Climate fluctuations of tropical coupled systems - The role of ocean dynamics. *J. Climate,* **19**, 5122–5174.

Chang, P., L. Zhang, R. Saravanan, D. J. Vimont, J. C. H. Chiang, L. Ji, H. Seidel, and M. K. Tippett, (2007) Pacific meridional mode and El Niño–Southern Oscillation. *Geophys. Res. Lett.*, **34**, L16608, doi:10.1029/2007GL030302.

Chiang, J. C. H., and D. J. Vimont (2004) Analogous Pacific and Atlantic meridional modes of tropical atmosphere–ocean variability. *J. Climate*, **17**, 4143–4158.

Chiodi, A.M., and E. Harrison (2007) Mechanisms of Summertime Subtropical Southern Indian Ocean Sea Surface Temperature Variability: On the Importance of Humidity Anomalies and the Meridional Advection of Water Vapor. *J. Climate*, 20, 4835-4852.

Clarke, A.J., and S. Van Gorder (2003) Improving El Niño Prediction using a Space-Time Integration of Indo-Pacific Winds and Equatorial Pacific Upper Ocean Heat Content. *Geophys. Res. Lett.*, **30**, 52.1-52.4.

Cleveland, R.B., W. S. Cleveland, J. E. McRae, and I. Terpenning (1990) A Seasonal-Trend Decomposition Procedure Based on Loess (with Discussion) . *Journal of Official Statistics*, 6, 3-73.

de Boyer Montégut, C., G. Madec, A. S. Fischer, A. Lazar, and D. Iudicone (2004) Mixed layer depth over the global ocean: an examination of profile data and a profile-based climatology, *J. Geophys. Res.*, *109*, C12003, doi:10.1029/2004JC002378

Deser, C., M.A. Alexander and M.S. Timlin (2003) On the persistence of sea surface temperature anomalies in midlatitudes. *J. Climate*, 16, 57-72.

Dominiak S. and P. Terray (2005) Improvement of ENSO prediction using a linear regression model with a Southern Indian Ocean Sea Surface Temperature Predictor. *Geophys. Res. Lett.*, **32**, L18702, doi:10.1029/2005GL023153.

Dommenget, D., V. Semenov, and M. Latif (2006) Impacts of the tropical Indian and Atlantic Oceans on ENSO. *Geophys. Res. Lett.*, **33**, L11701, doi:10.1029/2006GL025871.

Ebisuzaki, W. (1997) A method to estimate the statistical significance of a correlation when the data are serially correlated. *J. Climate*, **10**, 2147-2153.

England, M.H., C.C. Ummenhofer, and A. Santoso (2006) Interannual rainfall extremes over southwest West Australia linked to Indian Ocean climate variability. *J. Climate*, **19**, 1948-1969.

Fauchereau, N., S. Trzaska, Y. Richard, P. Roucou and P. Camberlin (2003) Sea-Surface Temperature co-variability in the southern Atlantic and Indian oceans and its connections with the atmospheric circulation in the Southern Hemisphere. *Int. J. Climatol.*, **23**, 663-677.

Florenchie, P., C.J.C. Reason, J.R.E. Lutjeharms, M. Rouault, C. Roy and S. Masson (2004) Evolution of Interannual Warm and Cold Events in the Southeast Atlantic Ocean. *J. Climate*, **17**, 2318-2334.

Flugel, M., P. Chang, and C. Penland (2004) The role of stochastic forcing in modulating ENSO predictability. *J. Climate*, **17,** 3125–3140.

Gill, A.E. (1980) Some simple solutions for the heat induced tropical circulation. *Q. J. Met. Soc*., 106,447–462.

Gillet, N.P., and D.W.J. Thomson (2003) Simulation of recent Southern Hemisphere climate change. *Science*, 302, 273-275.

Graham, N.E., and T.P. Barnett (1987) Sea surface temperature, surface wind divergence and convection over tropical Oceans. *Science*, **238**, 657-659.

Hall, A., and M. Visbeck (2002) Synchronous variability in the Southern Hemisphere atmosphere, sea ice, and ocean resulting from the annular mode. *J. Climate*, **15**, 3043-4395.

Hermes, J.C., and C.J.C. Reason (2005) Ocean model diagnosis of interannual coevolving SST Variability in the South Indian and South Atlantic Oceans. *J. Climate*, **18**, 2864–2882.

Hobbs, W. R., and M. N. Raphael (2007) A representative time-series for the Southern

Hemisphere zonal wave 1. *Geophys. Res. Lett.*, **34,** L05702.

Huang, B., and J. Shukla (2006) Interannual SST Variability in the Southern Subtropical and Extra-tropical Ocean. *COLA Tech. Report*, 223, 20 pp.

Huang, B., and J. Shukla (2007) Interannual Variability of the South Indian Ocean in Observations and a Coupled Model. *COLA Tech. Report*, 235, 49 pp.

Izumo, T., J. Vialard, M. Lengaigne, C. de Boyer Montegut, S.K. Behera, J.J. Luo, S. Cravatte, S. Masson and T. Yamagata (2010) Influence of the state of the Indian Ocean Dipole on the following year's El Niño. Nature Geoscience 3, 168–172 doi:10.1038/ngeo760.

Jansen, M.F., D. Dommenget, and N. Keenlyside (2009) Tropical Atmosphere-Ocean Interactions in a Conceptual Framework. *J. Climate*, 22, 550-567.

Jin, D., and B. Kirtman (2009) Why the Southern Hemisphere ENSO responses lead ENSO, J. Geophys. Res., 114, D23101, doi:10.1029/2009JD012657.

Jin, E. K., and Coauthors (2008) Current status of ENSO prediction skill in coupled ocean–atmosphere models. *Clim., Dyn*., **31,** 647-664.

Kalnay, E., M. Kanamitsu, R. Kistler, W. Collins, D. Deaven, L. Gandin, M. Iredell, S. Saha, G. White, J. Woollen, Y. Zhu, M. Chelliah, W. Ebisuzaki, W. Higgins, J. Janowiak, K. C. Mo, C. Ropelewski, J. Wang, A. Leetmaa, R. Reynolds, R. Jenne, and D. Joseph (1996) The NCEP/NCAR 40-year reanalysis project. *Bull. Amer. Met. Soc.*, **77**, 437-471.

Kanamitsu, M., W. Ebisuzaki, J. Woolen, J. Potter, S-K Yang, J.J. Hnilo, M. Fiorino, and G. L. Potter (2002) NCEP-DEO AMIP-II Reanalysis (R-2). *Bull. Amer. Met. Soc.*, **83,** 1631–1643.

Karoly, D. J. (1989) Southern hemisphere circulation features associated with El Niño-Southern Oscillation events. *J. Climate*, **2,** 1239-1252.

Kessler, W. S. (2002) Is ENSO a cycle or a series of events? *Geophys. Res. Lett.*, **29,** 2125,

doi:10.1029/2002GL015924.

Kidson, J.W., (1999) Principal modes of Southern Hemisphere low-frequency variability obtained from NCEP-NCAR reanalyses. *J. Climate*, **12**, 2808-2830.

Kidson, J. W., and J. A. Renwick (2002) The southern hemisphere evolution of ENSO during 1981-99. *J. Climate*, **15**, 847-863.

Kug, J.-S., S.-I1 An, F.-F. Jin, and I.-S. Kang (2005) Preconditions for El Niño and La Niña onsets and their relation to the Indian Ocean. *Geophys. Res. Lett.*, **32,** L05706, doi:10.1029/2004GL021674.

Kug, J. S., and I. S. Kang (2006) Interactive feedback between ENSO and the Indian Ocean. *J. Climate*, **19**, 1784-1801.

Kug, J. S., B. Kirtman, and I. S. Kang (2006) Interactive Feedback between ENSO and the Indian Ocean in an Interactive Ensemble Coupled Model. *J. Climate*, 19, 6371-6381.

Kwok, R., and J.C. Comiso (2002) Southern Ocean Climate and Sea Ice Anomalies Associated with the Southern Oscillation. *J. Climate*, **15**, 487-501.

Lau, K.M, H.T. Wu, and S. Bony (1997) The role of large-scale atmospheric circulation in the relationship between tropical convection and sea surface temperature. *J. Climate*, **10**, 381-392.

Lau, K. M., and P. H. Chan (1988) Intraseasonal and interannual variations of tropical convection: A possible link between the 40–50 day oscillation and ENSO. *J. Atmos. Sci.*, **45,** 506–521.

Lau, N.C., and M.J. Nath (2000) Impact of ENSO on the variability of the Asian-Australian monsoons as simulated in GCM experiments. *J. Climate*, **13**, 4287-4309.

Lau N.C. and M.J. Nath (2003) Atmosphere-Ocean Variations in the Indo-Pacific Sector during ENSO Episodes. *J. Climate*, **16**, 3-20.

Liebmann, B., and C.A. Smith (1996) Description of a complete (interpolated) outgoing longwave radiation dataset. *Bull. Amer. Meteor. Soc.*, **77**, 1275-1277.

Lindzen, R.S., and S. Nigam (1987) On the role of sea surface temperature gradients in forcing low-level winds and convergence in the Tropics. *J. Atmos. Sci.*, **44**, 2418-2436.

Luo, J.J., R. Zhang, S. Behera, Y. Masumoto, F.F. Jin, R. Lukas and T. Yamagata (2009) Interaction between El Niño and Extreme Indian Ocean Dipole. *J. Climate*, in press.

L'Heureux, M. L., and D. W. J. Thompson (2006) Observed relationships between the El Niño-Southern Oscillation and the extratropical zonal-mean circulation. *J. Climate*, **19,** 276-287.

McPhaden, M. J., X. Zhang, H. H. Hendon, and M. C. Wheeler (2006) Large scale dynamics and MJO forcing of ENSO variability. *Geophys. Res. Lett.*, **33,** L16702, doi:10.1029/2006GL026786.

Mo, K. C. (2000) Relationships between low-frequency variability in the southern hemisphere and sea surface temperature anomalies. *J. Climate*, **13,** 3599-3610.

Moore, A. M., and R. Kleeman (1999) Stochastic forcing of ENSO by the intraseasonal oscillation. *J. Climate,* **12,** 1199–1220.

Morioka, Y., T. Tozuka and T. Yamagata (2009) Climate variability in the Southern Indian Ocean as revealed by self-organizing maps. *Climate Dyn.*, submitted.

Penland, C., and L. Matrasova (2006) Studies of El Niño and inerdecadal variability in tropical sea surface temperatures using a nonnormal filter. J. Climate, 19, 5796-5815.

Penland, C., and L. Matrasova (2008) A Southern Hemisphere footprint in American Midwest precipitation. *Geophys. Res. Lett*., **35**, L09703, doi:10.1029/2008GL033612.

Peterson, R., and W.B. White (1998) Slow oceanic teleconnections linking tropical ENSO and the Antarctic circumpolar wave. *J. Geophys. Res.*, **103**, 24,573-24,583.

Rayner, N.A., Parker, D.E., Horton, E.B., Folland, C.K., Alexander, L.V., Rowell, D.P., Kent, E.C., and A. Kaplan (2003) Global analyses of sea surface temperature, sea ice, and night marine air temperature since the late nineteenth century. *J. Geophys. Res.*, **108** (D14), 4407, doi:10.1029/2002JD002670.

Renwick, J.A. (2005) Persistent positive anomalies in the Southern Hemisphere circulation. *J. Climate*, **133**, 977-988.

Ribera, P., and M.E. Mann (2003) ENSO related variability in the Southern Hemisphere, 1948-2000. *Geophys. Res. Lett.*, doi :10.1029/2002GL015818.

Rodriguez-Fonseca, B., I. Polo, J. Garcia-Serrano, T. Losada, E. Mohino, C. R. Mechoso, and F. Kucharski (2009) Are Atlantic Niños enhancing Pacific ENSO events in recent decades?, *Geophys. Res. Lett.*, doi:10.1029/2009GL040048, in press.

Sara, S., and Coauthors (2006) The NCEP climate forecast system. *J. Climate*, **19,** 3483-3517.

Sterl, A., and W. Hazeleger (2003) Coupled variability and air-sea interaction in the South Atlantic Ocean. *Clim., Dyn.*, **21**, 559-571.

Suzuki, R., S.K. Behera, S. Iizuka, T. Yamagata (2004) Indian Ocean subtropical dipole simulated using a coupled general circulation model. *J. Geophy. Res.*, 109, doi:10.1029/2003JC001974.

Terray, P., and S. Dominiak (2005) Indian Ocean Sea Surface Temperature and El Niño-Southern Oscillation: a new perspective. *J. Climate*, **18**, 1351-1368.

Terray, P., S. Dominiak, and P. Delecluse (2005) Role of the southern Indian Ocean in the transitions of the monsoon-ENSO system during recent decades. *Clim., Dyn.*, **24**, 169-195, DOI: 10.1007/s00382-004-0480-3.

Terray P., F. Chauvin et H. Douville (2007) Impact of southeast Indian Ocean Sea Surface Temperature anomalies on monsoon-ENSO-dipole variability in a coupled ocean-atmosphere model. *Clim., Dyn.*, **28**, 553-580, DOI: 10.1007/s00382-006-0192-y.

Thompson, D. W. J., and J. M. Wallace, 2000) Annular modes in the extratropical circulation. Part I: Month-to-Month variability. *J. Climate*, **13,** 1000-1016.

Toniazzo, T. (2009) Climate variability in the south-eastern tropical Pacific and its relation with ENSO: a GCM study. *Clim., Dyn.,* DOI: 10.1007/s00382-009-0602-z.

Torrence C., and P. Compo (1998) A practical guide to Wavelet Analysis. *Bull. Amer. Meteor. Soc.*, **79**, 61-78.

Trenberth, K.E., and K.C. Mo (1985) Blocking in the Southern Hemisphere. *Mon. Wea. Rev.*, 113, 3-21.

Trenberth, K. E., G. W. Branstator, D. Karoly, A. Kumar, N.-C. Lau, and C. Ropelewski (1998) Progress during TOGA in understanding and modelling global teleconnections associated with tropical sea surface temperatures. *J. Geophys. Res.*, **103**, 14 291–14 324.

Trenberth, K.E., J.M. Caron, D.P. Stepaniak, and S. Worley (2002) The evolution of ENSO and global atmospheric surface temperatures. *J. Geophys. Res.*, **107**, D8, 10.1029/2000JD000298.

Tziperman, E.,and L. Yu (2007) Quantifying the dependence of westerly wind birsts on the large-scale tropical Pacific SST. *J. Climate*, **20**, 2760-2768.

Uppala, S., and Coauthors (2005) The ERA-40 re-analysis. *Quart. J. Roy. Meteor. Soc.*, **131,** 2961–3012.

Van Loon, H. (1984) The Southern Oscillation. Part III: Associations with the trades and with the trough in the westerlies of the South Pacific Ocean. *Mon. Wea. Rev.*, **112**, 947-954.

Van Loon, H., and D.J. Shea (1987) The Southern Oscillation. Part VI: Anomalies of sea level pressure on the Southern Hemisphere and of Pacific sea surface temperature during the development of a warm event, *Mon. Wea. Rev.*, **115**, 370-379.

Venegas, S.A., L.A. Mysak, and D.N. Straub (1997) Atmosphere–ocean coupled variability in the South Atlantic. *J. Climate*, **10**, 2904–2920.

Vimont, D.J., D. S. Battisti, and A. C. Hirst (2001) Footprinting: A seasonal connection between the tropics and mid-latitudes. *Geophys. Res. Lett.*, **28**, 3923–3926.

Vimont, D.J., J. M. Wallace, and D. S. Battisti (2003) The seasonal footprinting mechanism in the Pacific: Implications for ENSO. *J. Climate*, **16**, 2668–2675.

Vimont, D.J., M. Alexander and A. Fontaine (2009) Midlatitude Excitation of Tropical Variability in the Pacific: The Role of Thermodynamic Coupling and Seasonality. *J. Climate*, **22**, 518-534.

Wang, C. (2006) An overlooked feature of tropical climate: Inter-Pacific-Atlantic variability. *Geophys. Res. Lett.*, **33**, L12702, doi:10.1029/2006GL026324.

Watanabe, M., and F.-F. Jin (2002) Role of Indian Ocean warming in the development of Philippine Sea anticyclone during ENSO. *Geophys. Res. Lett.*, **29**, doi: 10.1029/2001GL014318.

Welch, P.D. (1967) The use of Fast Fourier Transform for the estimation of power spectra: a method based on time averaging over short, modified periodograms. *IEEE Transactions on Audio and Electroacoustics*, Vol. 15, 2, 70-73.

White, W.B., S.-C Chen, R.J. Allan, and R.C. Stone (2002) Positive feedbacks between the Antarctic Circumpolar Wave and the global El Niño-Southern Oscillation Wave. *J. Geophys. Res.*, **107**(C10), 3165, doi:10.1029/2000JC000581.

White, W.B., and J. Annis (2004) Influence of the Antarctic Circumpolar Wave on El Niño and its multidecadal changes from 1950-2001. *J. Geophys. Res.*, **109**(C0), 6019, doi:10.1029/2002JC001666.

Wright, P. B. (1986) Precursors of the Southern Oscillation, *J. Climatol.*, **6**, 17– 30.

Wu, R. G. and B. P. Kirtman (2004) Understanding the impacts of the Indian Ocean on ENSO variability in a coupled GCM. *J. Climate*, **17**, 4019-4031.

Xie, S.-P., and S. G. H. Philander (1994) A coupled ocean–atmosphere model of relevance to the ITCZ in the eastern Pacific. Tellus, **46**A, 340–350.

Yu, J.-Y., C. R. Mechoso, J. C. McWilliams, and A. Arakawa (2002) Impacts of the Indian Ocean on the ENSO cycle. *Geophys. Res. Lett.*, **29,** 1204 10.1029/2001GL014098.

Yu, L., X. Jin, and R. A. Weller (2008) Multidecade Global Flux Datasets from the Objectively Analyzed Air-sea Fluxes (OAFlux) Project: Latent and sensible heat fluxes, ocean evaporation, and related surface meteorological variables. Woods Hole Oceanographic Institution, *OAFlux Project Technical Report*. OA-2008-01, 64pp. Woods Hole. Massachusetts.

Zhang, Y., J.R. Norris, and J.M. Wallace (1998) Seasonality of large-scale atmosphere-ocean interaction over the North Pacific. *J. Climate*, **11**, 2473-2481.

Figure captions:

Figure 1: Power spectra of the raw bi-monthly Niño34 SST time series (black line) and of the average of STL residual components of bi-monthly SST time series (blue line) in the Niño34 region during the 1870-2006 period. The bottom axis is the period (unit: year), the left axis is variance (unit: $°C^2$) and both axes are in logarithm scale. The power spectrum is estimated using a FFT algorithm on overlapping segments (Welch, 1967).

Figure 2: Bi-monthly standard deviations of interannual SST anomalies as computed from STL residuals for the period 1979-2006.). Contour interval is 0.1°C.

Figure 3: Spatial patterns of the first EOF of bi-monthly SST anomaly fields over the South Pacific Oceans during (a) December-January and (b) February-March, the South Indian Ocean during (c) December-January and (d) February-March and the South Atlantic Ocean during (e) December-January and (f) February-March. The number in parentheses in the heading of each panel shows the percentage of variance accounted for by the mode during the 1979-2006 period.

Figure 4: Same as in Figure 3, but for (a) a circumpolar domain between 10-50°S of latitude during December-January and (b) a combined South Atlantic-Indian domain (10-50°S, 50°W-150°E) during February-March.

Figure 5: Correlation SLP maps of the leading SVD modes for SLP paired with SST in December-February and February-March: (a) and (b) over the South Pacific Ocean, (c) and (d) over the South Indian Ocean and, (e) and (f) over the South Atlantic Ocean. The number in parentheses in the heading of each panel shows the Squared Covariance Fraction accounted for by the SVD mode during the 1979-2004 period. The black contours denote the correlation coefficients above the 90% confidence level according to a phase-scrambling statistical test (see Section 2). The convention for the color shading is indicated at the bottom of the panels.

Figure 6: Time expansion coefficients of the leading SST (yellow dashed curve) and SLP (dotted curve) SVD modes during December-January of the 1979-2004 period for (a) the South Pacific Ocean, (b) the South Indian Ocean and (c) the South Atlantic Ocean. The normalized December-January Niño34 SST index (red solid curve) is also shown on each panel. The correlation coefficients between the Niño34 SST index and the time expansion coefficients of the SST and SLP modes are also shown on the bottom of each panel.

Figure 7: As in Figure 6, but for the February-March season.

Figure 8: Homogeneous maps of the leading SVD mode for (a) SST paired with (b) SLP in December-February over a circumpolar domain between 10-50°S of latitude for SSTs and 10-70°S of latitude for SLPs during December-January; (c) and (d) same as (a) and (b), but for a combined South Atlantic-Indian domain during February-March. The number in parentheses in the heading of each panel shows the Squared Covariance Fraction accounted for by the SVD mode during the 1979-2004 period.

Figure 9: (a) Lead-lag correlations of bi-monthly Niño34 SST index with the leading SST EOF modes during December-January over the South Pacific, Indian, Atlantic, Pacific-Atlantic-Indian and Atlantic-Indian domains during the 1979-2006 period. The lags are in 2-months unit and lag 0 refers to the December-January season of the EOF modes. The closed circles indicate the correlation coefficients that are above the 95% confidence level as estimated by the phase-scrambling bootstrap test of Ebisuzaki (1997) with 999 samples. The correlations are computed beginning one year prior to the SST EOF modes and finishing two years after the SST EOF modes. (b) Same as (a) but for the leading SST SVD modes during December-January. (c) Same as (a) but for the leading SST EOF modes during February-March. (d) Same as (a) but for the leading SST SVD modes during February-March.

Figure 10: Time series of the normalized Niño34 SST index (red solid curve) during December-January and (a) the preceding February-March time expansion coefficients of the leading SST (yellow dashed curve) EOF mode over the combined South Atlantic-Indian domain ten months before. (b) Same as (a) but for the preceding February-March time expansion coefficients of the leading SST (yellow dashed curve) and SLP (dotted curve) SVD modes over the combined South Atlantic-Indian domain.

Figure 11: Time sequence of bi-monthly mean anomalies of SST (shading, unit: °C) obtained from regression of the SST fields on the time coefficient of the leading EOF mode of February-March SST fields over (a) the South Indian Ocean and (b) the South Atlantic Ocean. The time sequences are from -1 (December-January) to +3 (August-September) bi-monthly seasons. The SST dataset is from the OAFLUX product. The values plotted on the maps are in dimensional units and represent typical amplitudes of the global SST patterns associated with the occurrence of the subtropical dipole events. The contoured areas are significant at the 90% confidence level or better according to a phase-scrambling statistical test (see Section 2). The convention for the color shading is indicated at the bottom of the panels.

Figure 12: Time sequence of bi-monthly mean anomalies of SLP (shading, correlation) and 850 hPa wind (vector, scale shown at the bottom of the panels) obtained from correlation/regression of the SLP and wind fields on the time coefficient of the leading EOF mode of February-March SST fields over (a) the South Indian Ocean and (b) the South Atlantic Ocean. The time sequences are from -1 (December-January) to +3 (August-September) bi-monthly seasons. The SLP and 850 hPa wind fields are from the NCEP reanalysis. The maps only show regression/correlation coefficients that are above the 90% confidence level following a phase-scrambling procedure with 999 samples. The convention for the color shading is indicated at the bottom of the panels.

Figure 13: Time sequence of bi-monthly mean anomalies of OLR (shading, unit: Wm^{-2}) obtained from regression of the NOAA OLR fields on the time coefficient of the leading EOF mode of February-March SST fields over (a) the South Indian Ocean and (b) the South Atlantic Ocean. The time sequences are from -1 (December-January) to +3 (August-September) bi-monthly seasons. The black contours denote that the corresponding correlation coefficients are above the 90% confidence level. The convention for the color shading is indicated at the bottom of the panels.

Figure 14: Time sequence of bi-monthly mean anomalies of downward surface latent heat flux (shading, unit: Wm^{-2}) and surface (10m) wind obtained from regression of the fields on the time coefficient of the leading EOF mode of February-March SST fields over (a) the South Indian Ocean and (b) the South Atlantic Ocean. The time sequences are from -1 (December-January) to +1 (April-May) bi-monthly seasons. The convention used for latent heat flux is positive into the ocean so that the latent heat flux has a positive contribution to SST changes when the latent heat flux and SST anomalies have the same polarity. The maps only show regression/correlation coefficients that are above the 90% confidence level following a phase-scrambling procedure with 999 samples. The convention for the color shading is indicated at the bottom of the panels.

Figure 15: Time sequence of bi-monthly mean anomalies of downward surface net shortwave radiation (shading, unit: Wm^{-2}) obtained from regression of the fields on the time coefficient of the leading EOF mode of February-March SST fields over (a) the South Indian Ocean and (b) the South Atlantic Ocean. The time sequences are from -1 (December-January) to +1 (April-May) bi-monthly seasons. The convention used for the net shortwave radiation is positive into the ocean so that the net shortwave radiation has a positive contribution to SST changes when the net shortwave radiation and SST anomalies have the same polarity. The black contours denote the corresponding correlation coefficients that are above the 90% confidence level. The convention for the color shading is indicated at the bottom of the panels.

Figure 16: Distribution of the regression coefficients of April-May 400 (a) and 200 (b) hPa wind vectors (arrows, see scales below the panels) and of the correlation coefficients of 400 (a) and 200 (b) hPa temperature, 200-hPa velocity potential (c) and 200-hPa streamfunction (color shading) versus the time coefficients of the leading EOF mode of February-March SST fields over the combined South Atlantic-Indian domain. The fields are from the NCEP reanalysis. The convention for the color shading is indicated at the bottom of the panels. In the 200-hPa streamfunction correlation map, negative centers are anticyclonic in the Southern Hemisphere and cyclonic in Northern Hemisphere and vice-versa for positive centers. The maps only show regression/correlation coefficients that are above the 90% confidence level following a phase-scrambling procedure with 999 samples.

Figure 17: Longitude-height cross-sections along the Equator (4°S-4°N) of bi-monthly potential temperature anomalies obtained from regression of the fields on the time coefficient of the leading EOF mode of February-March SST fields over (a) the South Indian Ocean and (b) the South Atlantic Ocean. The time sequences are from 0 (February-March) to +5 (December-January) bi-monthly seasons. Pressure levels range linearly from 1000 to 150 hPa. The black contours denote the corresponding correlation coefficients that are above the 90% confidence level. The convention for the color shading is indicated at the bottom of the panels.

Table captions:

Table 1: Percentage eigenvalues of the first four modes of South Pacific, Indian and Atlantic SST EOF analyses during December-January and February-March seasons for the 1979-2006 period.

Table 2: Cross-correlations between the time coefficients of the leading EOF modes of South Pacific, Indian and Atlantic SSTs during December-January and February-March seasons for the 1979-2006 period. The coefficients exceeding the 1% and 1‰ probability levels according to the phase-scrambling bootstrap test of Ebisuzaki (1997) with 999 samples are followed by one star (*) and two stars (**), respectively.

Table 3: Summary statistics for the leading mode of the SVD analyses between SST and SLP fields during the December-January and February-March seasons of the 1979-2004 period and for the South Pacific, Indian and Atlantic Oceans, respectively. Here SCF is squared covariance fraction, NC is normalized root-mean-square and *r* is correlation of expansion coefficient time series or scores, as defined in the text; SSTvar and SLPvar are, respectively, SST and SLP variances accounted for by the leading mode of each SVD analysis.

TABLES

TABLE 1

December-January season

EOF mode/domain	Pacific	Indian	Atlantic
1	37.8	25.6	28.4
2	13.6	18.5	19.7
3	10.1	15.3	10.7
4	6.7	8.6	8.4

February-March season

EOF mode/domain	Pacific	Indian	Atlantic
1	31.7	33.6	33
2	15.1	15.7	19.5
3	13.6	10.9	12.1
4	8	8.8	7

TABLE 2

December-January season

Correlation	PAC SST EOF1	IO SST EOF1	AO SST EOF1
PAC SST EOF1	1		
IO SST EOF1	-0.58*	1	
AO SST EOF1	-0.73**	0.63**	1

February-March season

Correlation	PAC SST EOF1	IO SST EOF1	AO SST EOF1
PAC SST EOF1	1		
IO SST EOF1	-0.53*	1	
AO SST EOF1	-0.29	0.60**	1

TABLE 3

December-January season

	SCF (%)	NC (%)	r	SSTvar (%)	SLPvar(%)
Pacific SVD1	78.3	25.9	0.81	37.6	27.2
Indian SVD1	42.5	15.5	0.70	20.7	23.4
Atlantic SVD1	58.9	19.2	0.64	17.2	52.3

February-March season

	SCF (%)	NC (%)	r	SSTvar (%)	SLPvar(%)
Pacific SVD1	60.9	20.4	0.69	29.3	29.4
Indian SVD1	45.2	16.5	0.82	32.4	12.5
Atlantic SVD1	52.8	16.8	0.69	31.4	19.1

Figure 1

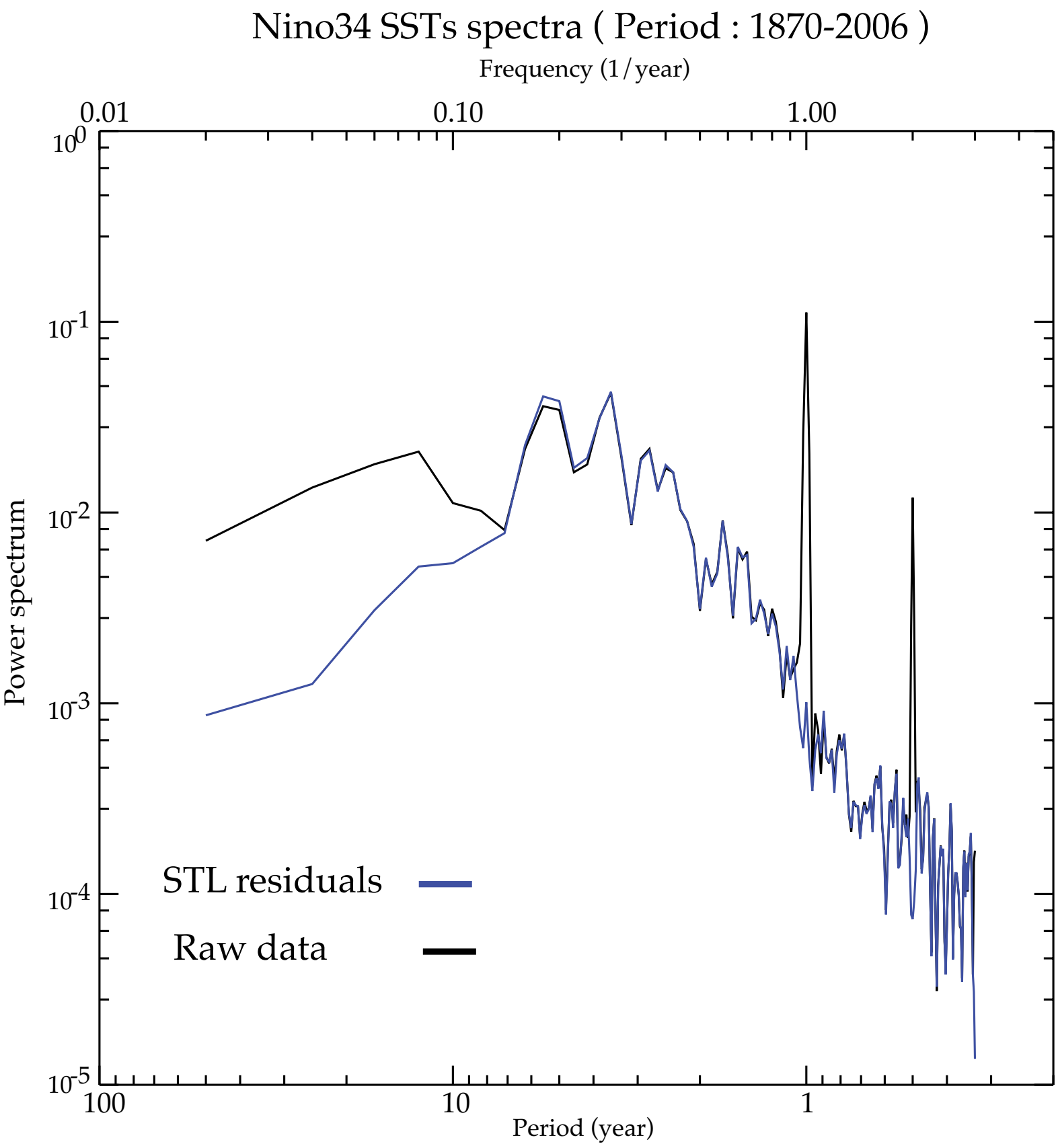
Nino34 SSTs spectra (Period : 1870-2006)
Frequency (1/year)
0.01
0.10
1.00
10^{0}
10^{-1}
10^{-2}
10^{-3}
10^{-4}
10^{-5}
Power spectrum
STL residuals
Raw data
100
10
1
Period (year)

Figure 2

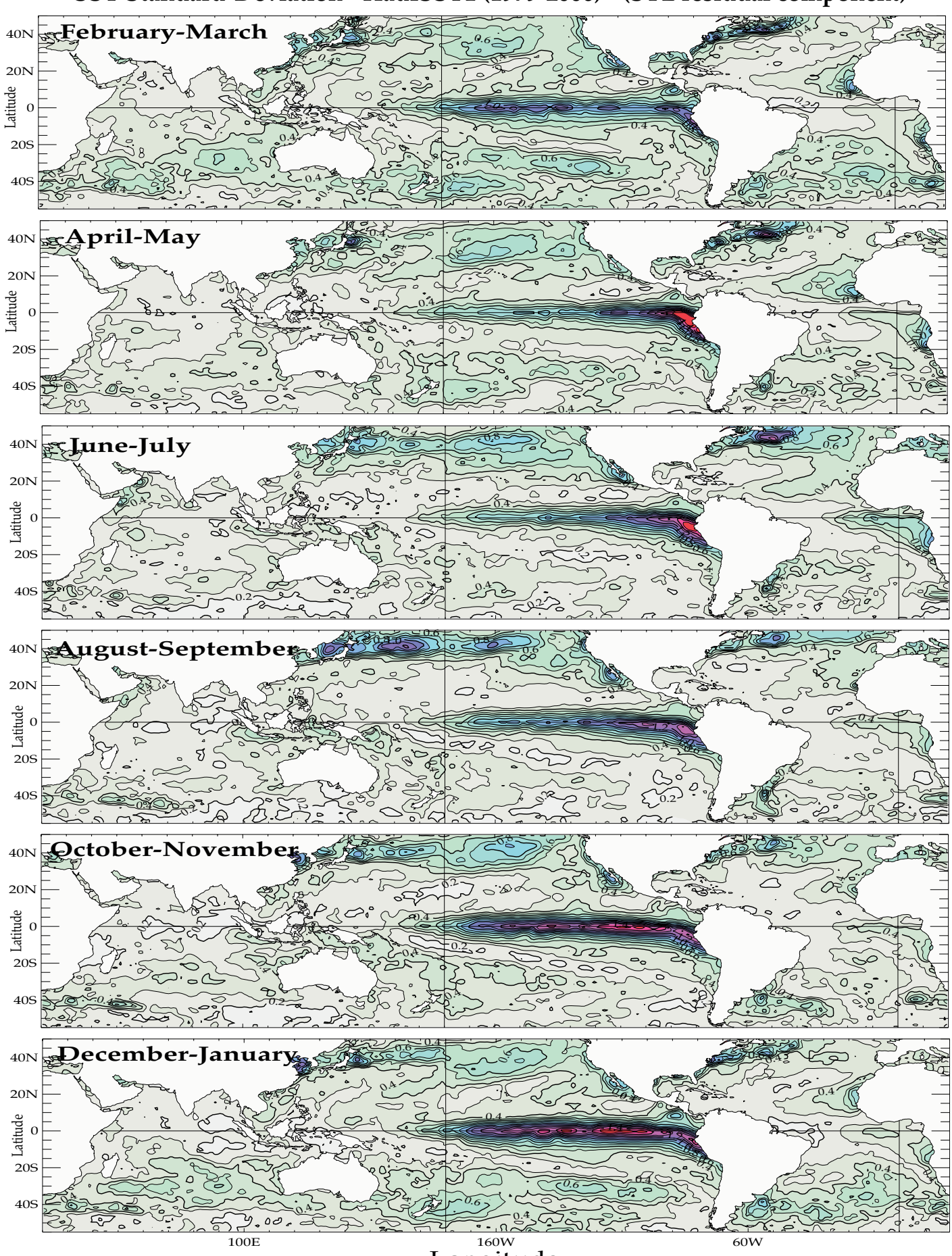
SST Standard-Deviation - HadISST1 (1979-2006) - (STL residual component)
February-March
April-May
June-July
August-September
October-November
December-January
40N
20N
0
20S
40S
Latitude
100E
160W
60W
Longitude
0.0
0.2
0.4
0.6
0.8
1.0
1.2
1.4
1.6
SST standard deviation (°C)

Figure 3

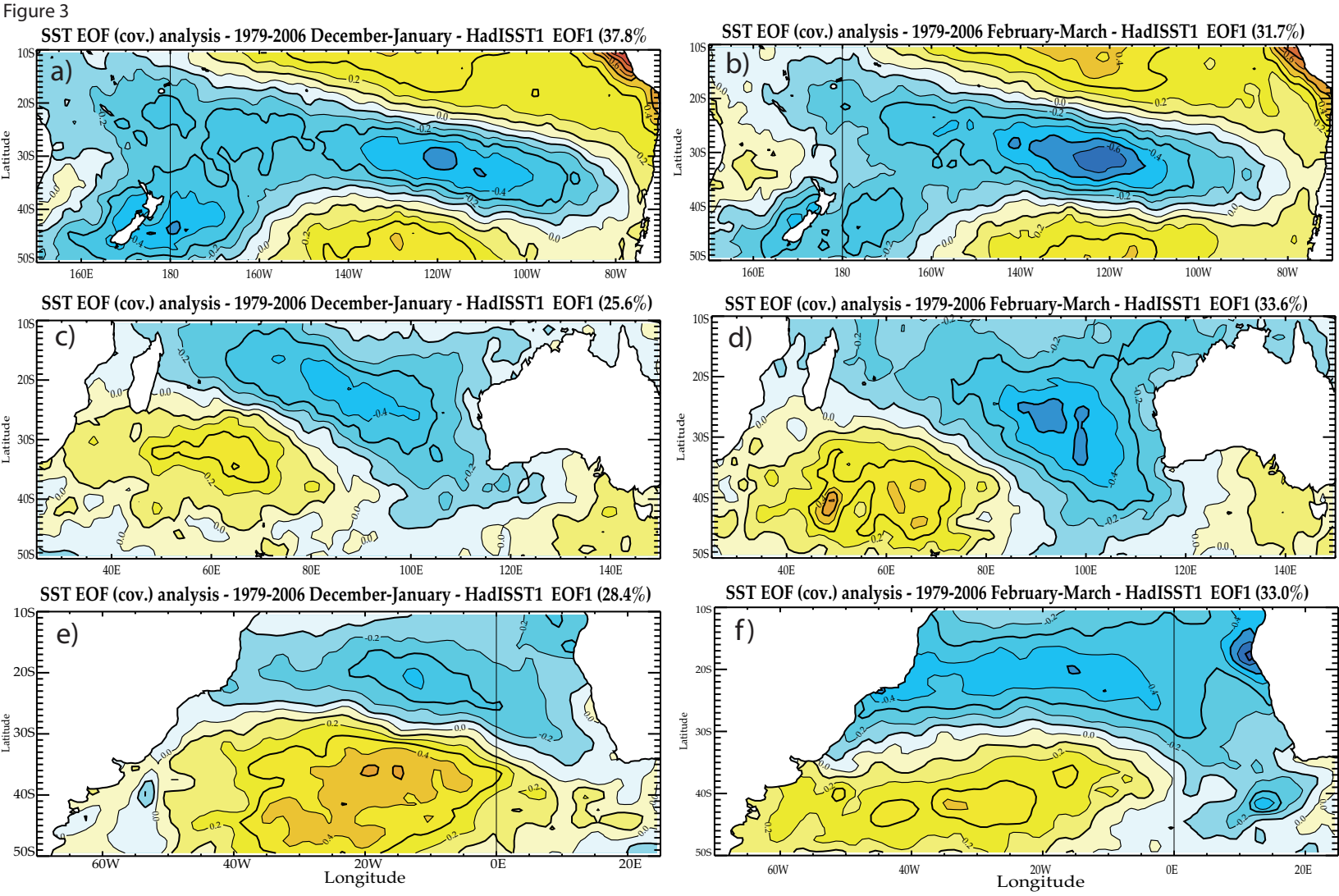
SST EOF (cov.) analysis - 1979-2006 December-January - HadISST1 EOF1 (37.8%
a)
SST EOF (cov.) analysis - 1979-2006 February-March - HadISST1 EOF1 (31.7%)
b)
SST EOF (cov.) analysis - 1979-2006 December-January - HadISST1 EOF1 (25.6%)
c)
SST EOF (cov.) analysis - 1979-2006 February-March - HadISST1 EOF1 (33.6%)
d)
SST EOF (cov.) analysis - 1979-2006 December-January - HadISST1 EOF1 (28.4%)
e)
SST EOF (cov.) analysis - 1979-2006 February-March - HadISST1 EOF1 (33.0%)
f)
Latitude
Longitude
-1.0 -0.8 -0.6 -0.4 -0.2 0.0 0.2 0.4 0.6 0.8 1.0
Covariance

Figure 4

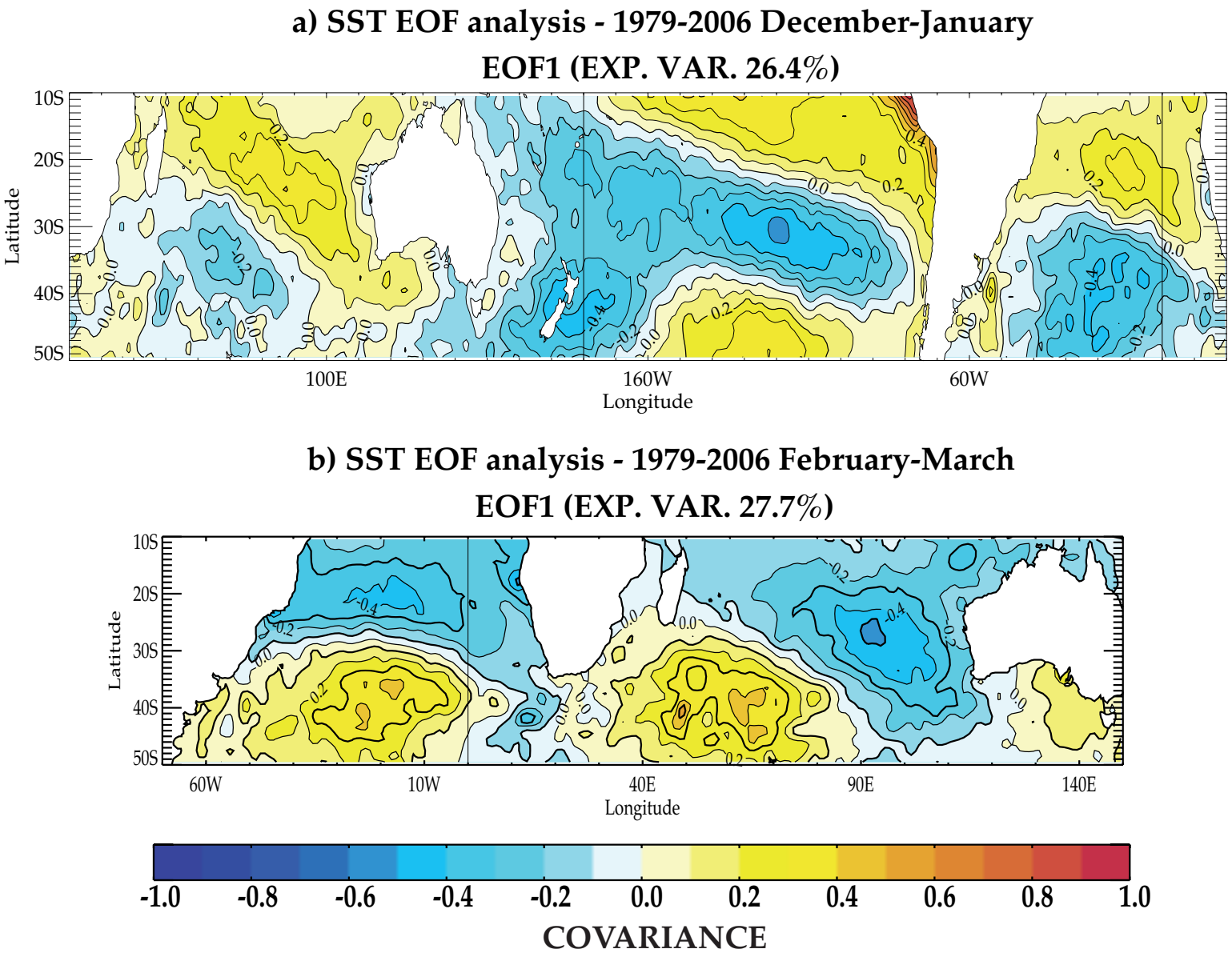
a) SST EOF analysis - 1979-2006 December-January
EOF1 (EXP. VAR. 26.4%)
10S
20S
30S
40S
50S
Latitude
100E
160W
60W
Longitude
b) SST EOF analysis - 1979-2006 February-March
EOF1 (EXP. VAR. 27.7%)
10S
20S
30S
40S
50S
Latitude
60W
10W
40E
90E
140E
Longitude
-1.0
-0.8
-0.6
-0.4
-0.2
0.0
0.2
0.4
0.6
0.8
1.0
COVARIANCE

Figure 5

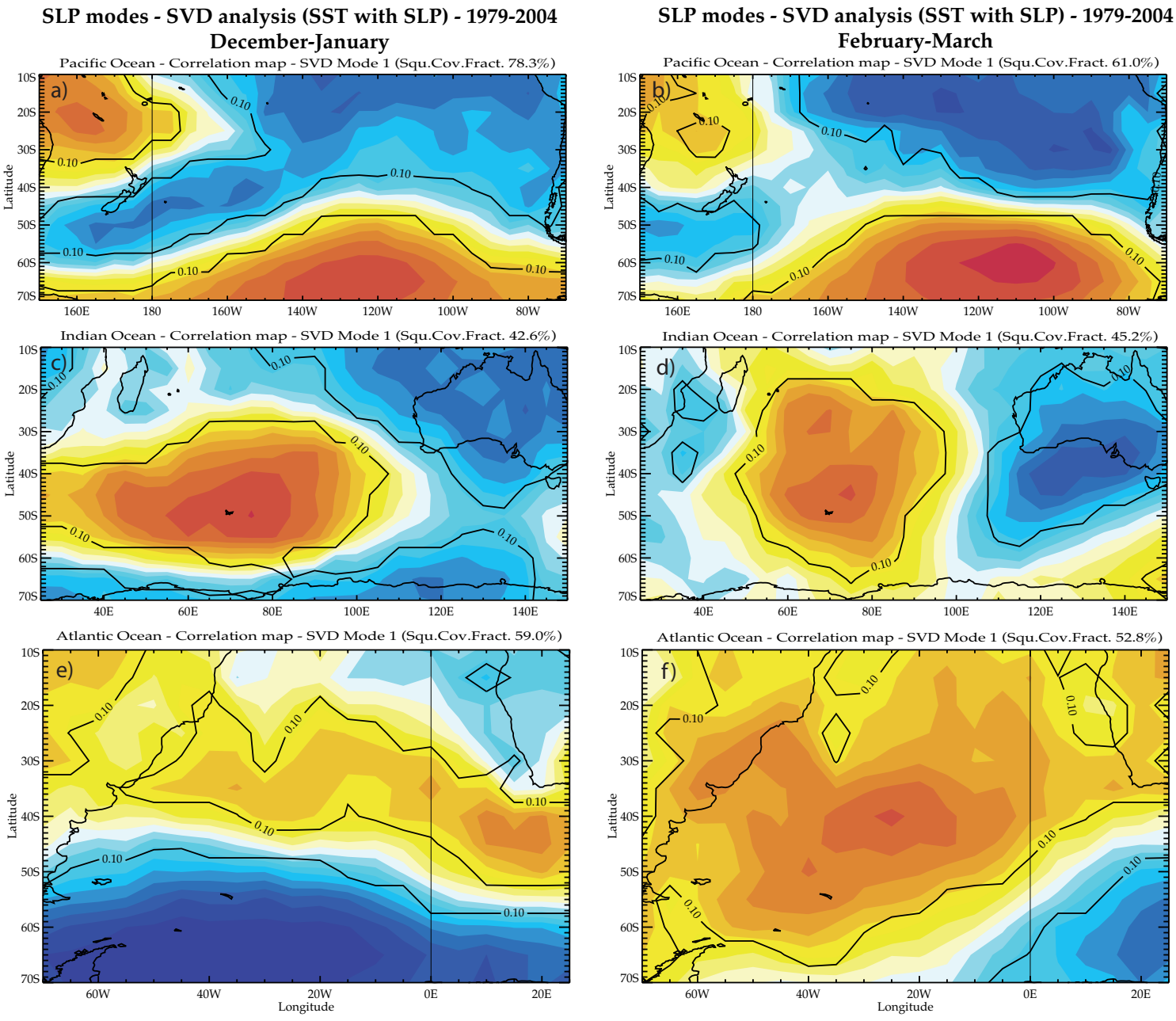
SLP modes - SVD analysis (SST with SLP) - 1979-2004
December-January
SLP modes - SVD analysis (SST with SLP) - 1979-2004
February-March
Pacific Ocean - Correlation map - SVD Mode 1 (Squ.Cov.Fract. 78.3%)
Pacific Ocean - Correlation map - SVD Mode 1 (Squ.Cov.Fract. 61.0%)
Indian Ocean - Correlation map - SVD Mode 1 (Squ.Cov.Fract. 42.6%)
Indian Ocean - Correlation map - SVD Mode 1 (Squ.Cov.Fract. 45.2%)
Atlantic Ocean - Correlation map - SVD Mode 1 (Squ.Cov.Fract. 59.0%)
Atlantic Ocean - Correlation map - SVD Mode 1 (Squ.Cov.Fract. 52.8%)
a)
b)
c)
d)
e)
f)
Latitude
Longitude
0.10
-1.0 -0.8 -0.6 -0.4 -0.2 0.0 0.2 0.4 0.6 0.8 1.0
CORRELATION

Figure 6

SVD analysis (SST with SLP) - 1979-2004 December-January

Standardized Singular Variables (SST SV1 dashed, SLP SV1 dotted) and Nino34 SST (12-1)

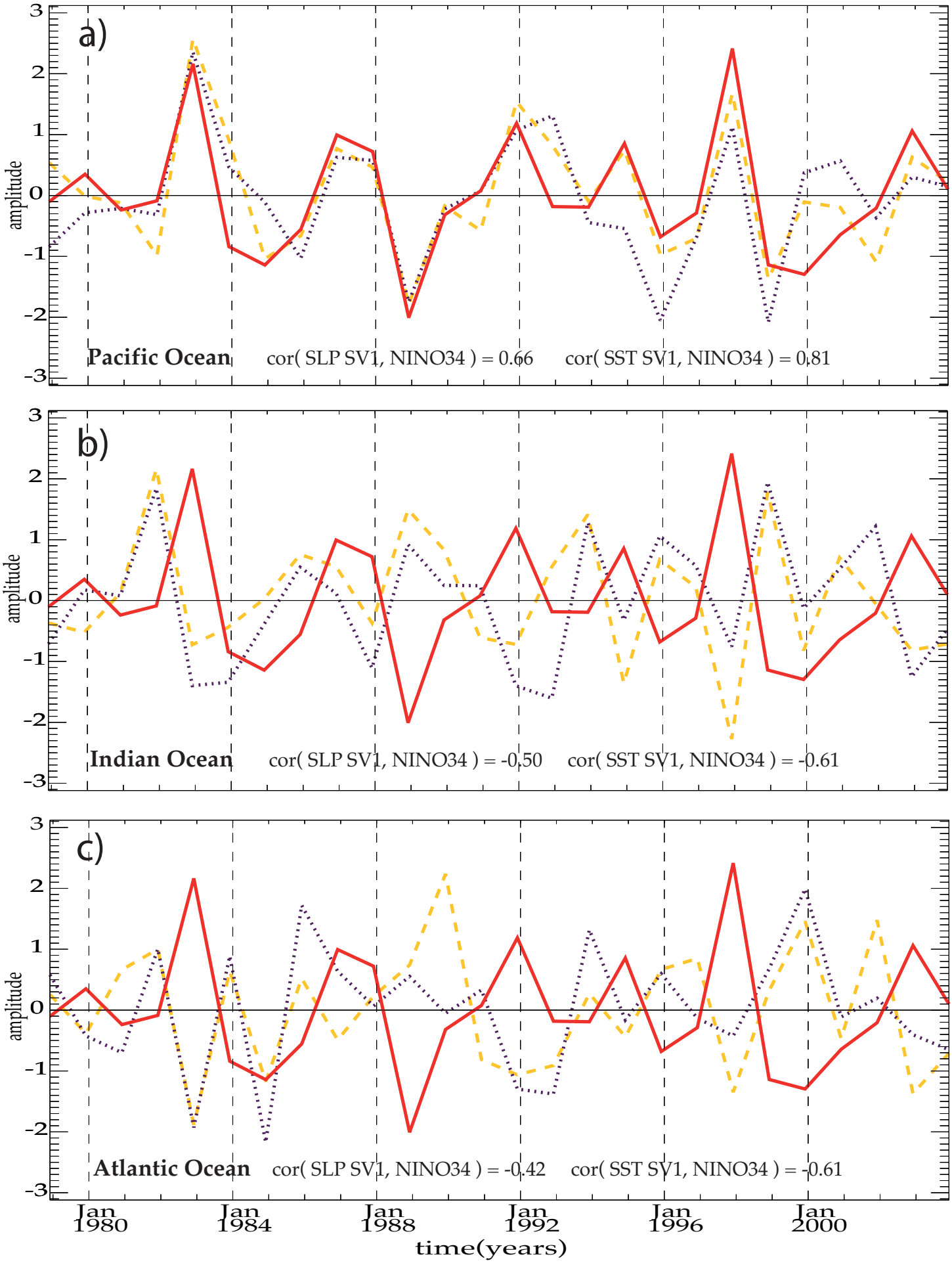

Figure 7

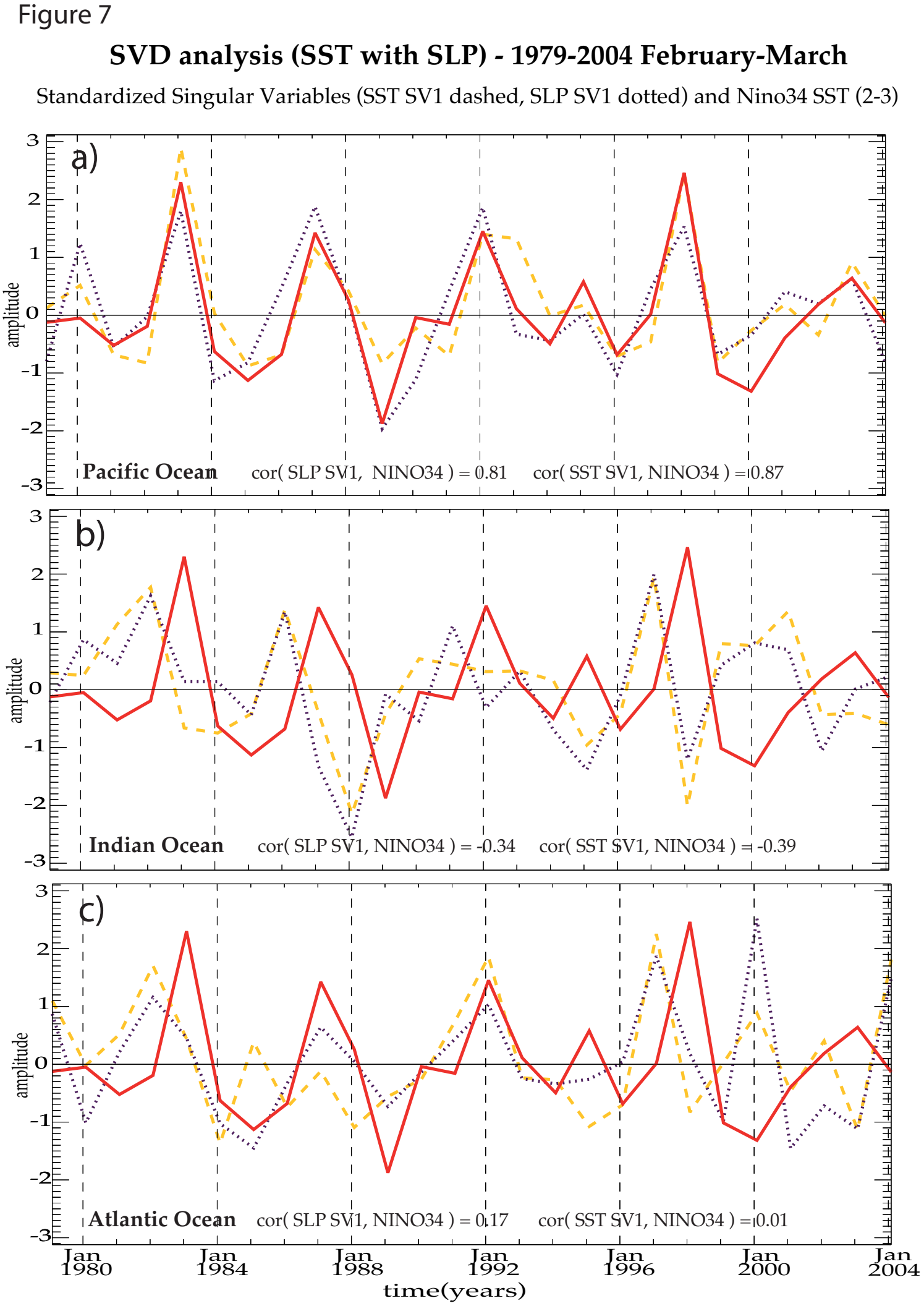
SVD analysis (SST with SLP) - 1979-2004 February-March
Standardized Singular Variables (SST SV1 dashed, SLP SV1 dotted) and Nino34 SST (2-3)
a)
amplitude
Pacific Ocean
cor(SLP SV1, NINO34) = 0.81
cor(SST SV1, NINO34) = 0.87
b)
amplitude
Indian Ocean
cor(SLP SV1, NINO34) = -0.34
cor(SST SV1, NINO34) = -0.39
c)
amplitude
Atlantic Ocean
cor(SLP SV1, NINO34) = 0.17
cor(SST SV1, NINO34) = 0.01
Jan 1980
Jan 1984
Jan 1988
Jan 1992
Jan 1996
Jan 2000
Jan 2004
time(years)

Figure 8

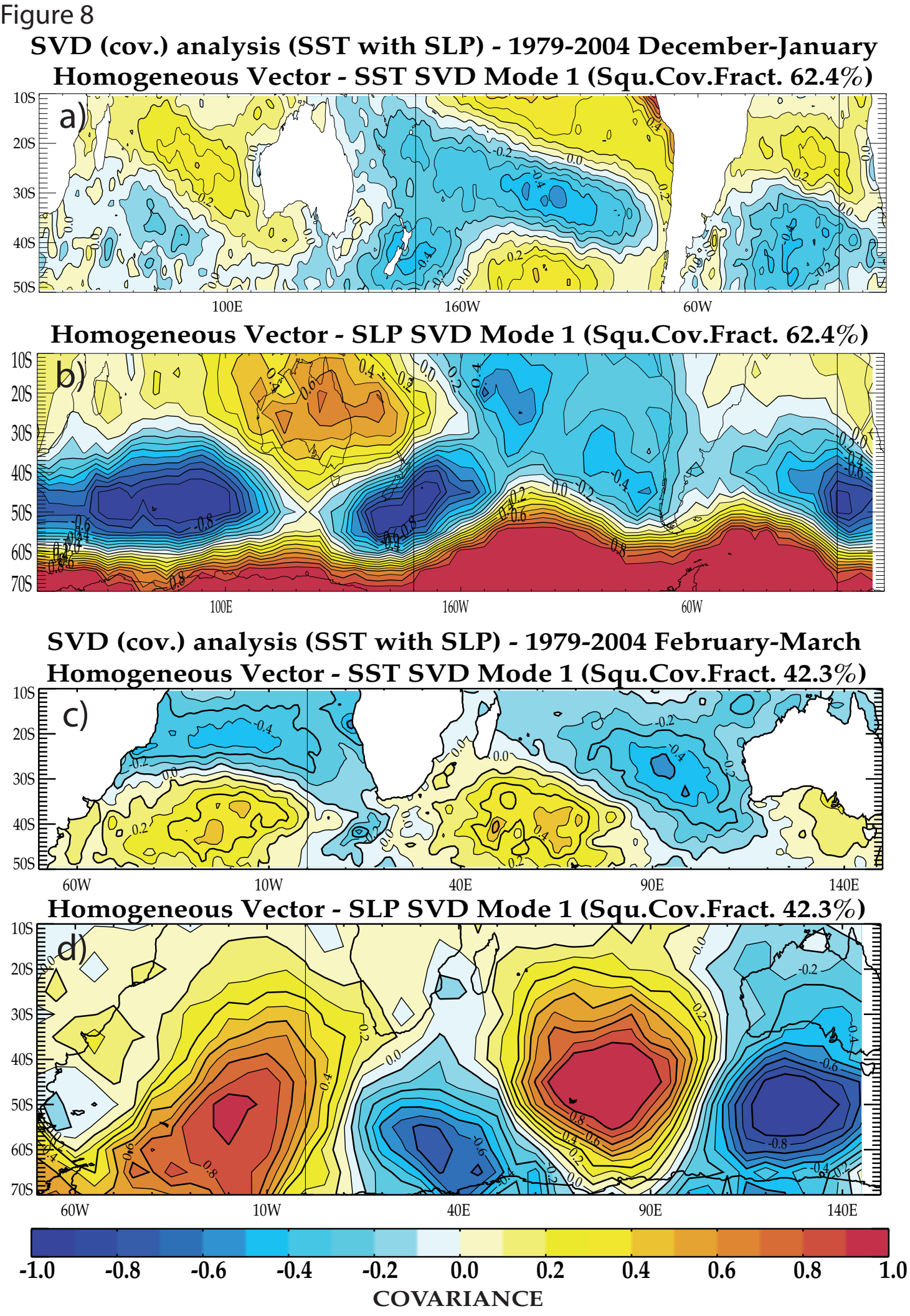
SVD (cov.) analysis (SST with SLP) - 1979-2004 December-January
Homogeneous Vector - SST SVD Mode 1 (Squ.Cov.Fract. 62.4%)
a)
10S
20S
30S
40S
50S
100E
160W
60W
Homogeneous Vector - SLP SVD Mode 1 (Squ.Cov.Fract. 62.4%)
b)
10S
20S
30S
40S
50S
60S
70S
100E
160W
60W
SVD (cov.) analysis (SST with SLP) - 1979-2004 February-March
Homogeneous Vector - SST SVD Mode 1 (Squ.Cov.Fract. 42.3%)
c)
10S
20S
30S
40S
50S
60W
10W
40E
90E
140E
Homogeneous Vector - SLP SVD Mode 1 (Squ.Cov.Fract. 42.3%)
d)
10S
20S
30S
40S
50S
60S
70S
60W
10W
40E
90E
140E
-1.0
-0.8
-0.6
-0.4
-0.2
0.0
0.2
0.4
0.6
0.8
1.0
COVARIANCE

Figure 9

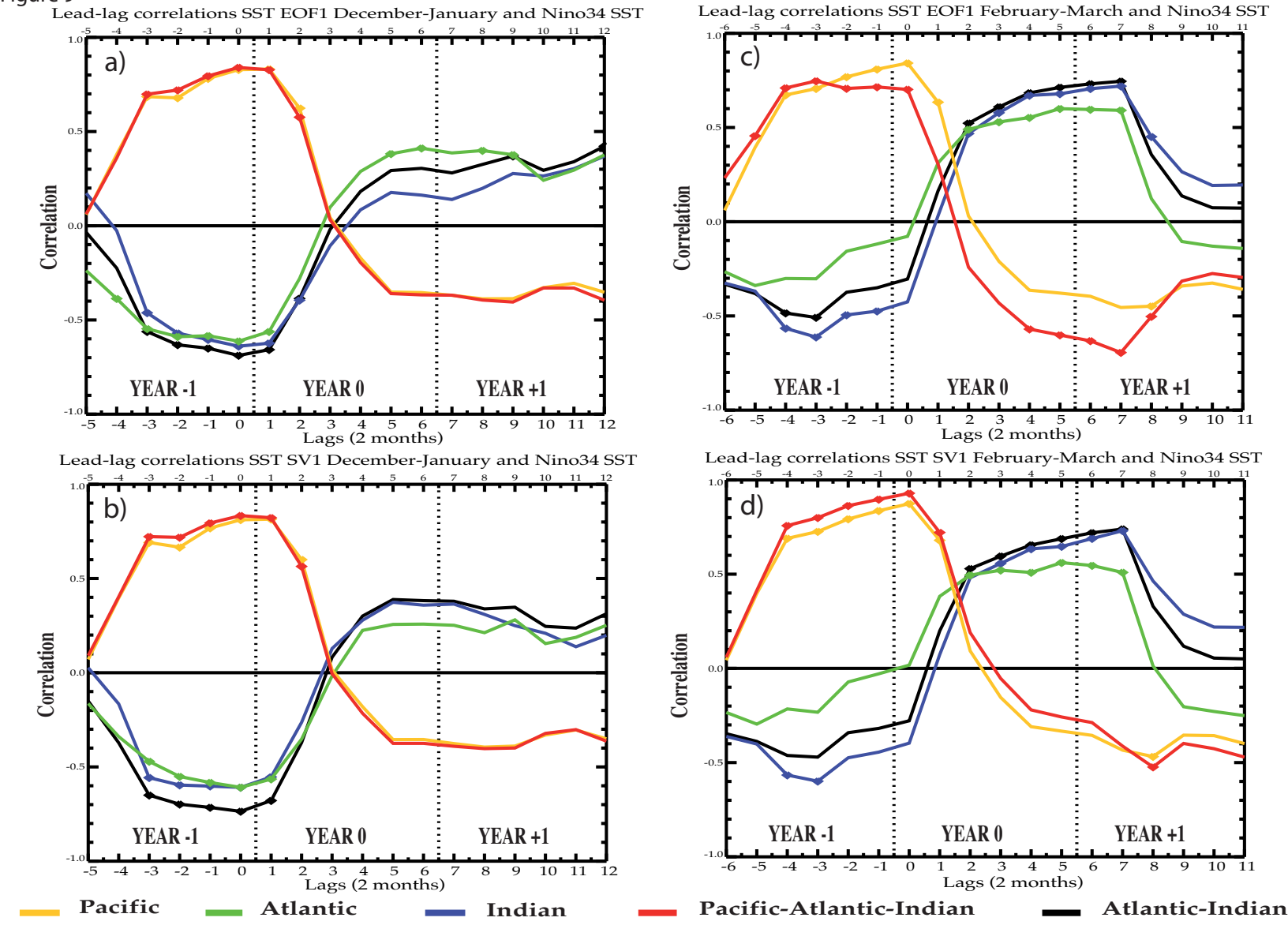
Lead-lag correlations SST EOF1 December-January and Nino34 SST
a)
Correlation
YEAR -1
YEAR 0
YEAR +1
Lags (2 months)
Lead-lag correlations SST EOF1 February-March and Nino34 SST
c)
Correlation
YEAR -1
YEAR 0
YEAR +1
Lags (2 months)
Lead-lag correlations SST SV1 December-January and Nino34 SST
b)
Correlation
YEAR -1
YEAR 0
YEAR +1
Lags (2 months)
Lead-lag correlations SST SV1 February-March and Nino34 SST
d)
Correlation
YEAR -1
YEAR 0
YEAR +1
Lags (2 months)
Pacific
Atlantic
Indian
Pacific-Atlantic-Indian
Atlantic-Indian

Figure 10

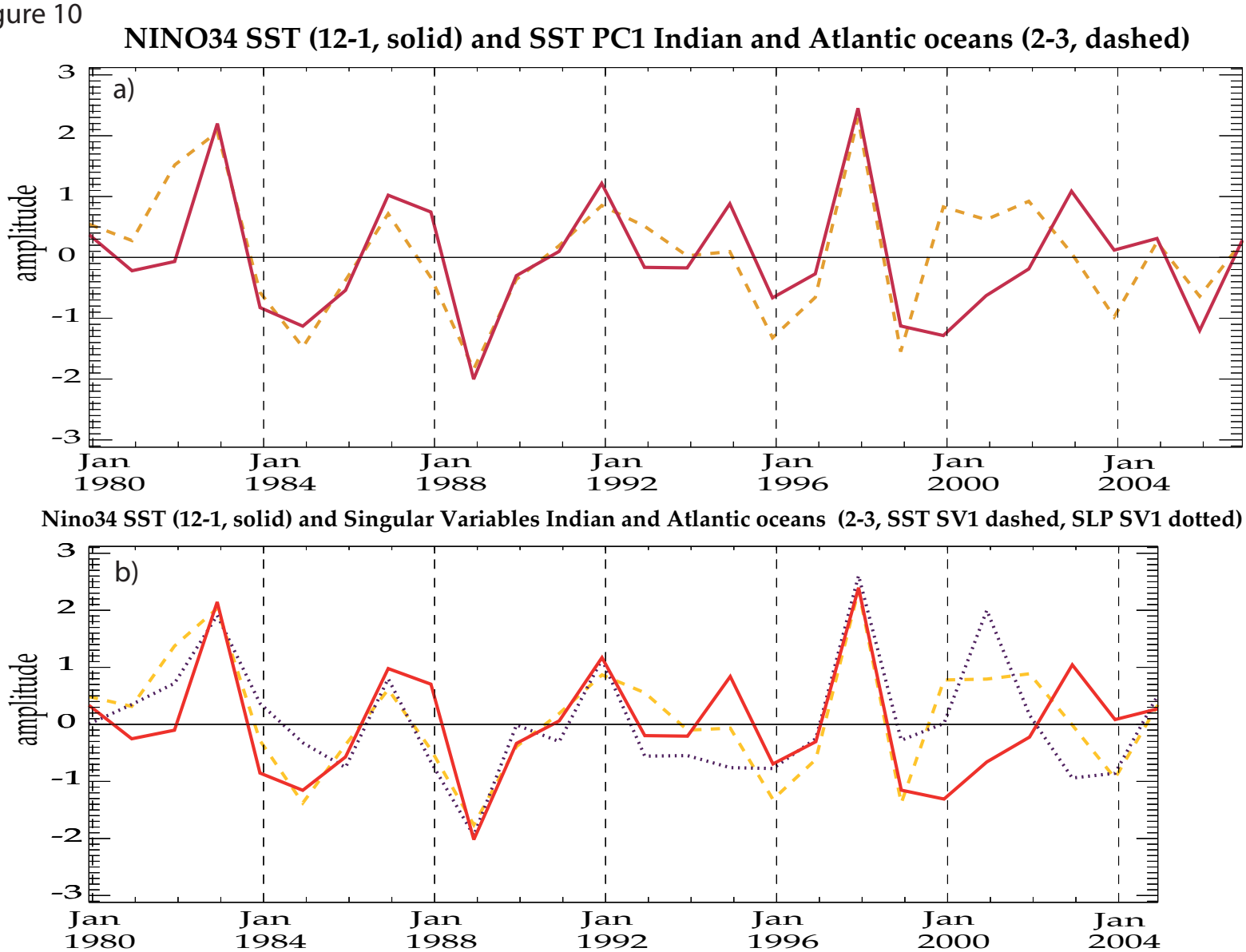
NINO34 SST (12-1, solid) and SST PC1 Indian and Atlantic oceans (2-3, dashed)
a)
amplitude
3
2
1
0
-1
-2
-3
Jan 1980
Jan 1984
Jan 1988
Jan 1992
Jan 1996
Jan 2000
Jan 2004
Nino34 SST (12-1, solid) and Singular Variables Indian and Atlantic oceans (2-3, SST SV1 dashed, SLP SV1 dotted)
b)
amplitude
3
2
1
0
-1
-2
-3
Jan 1980
Jan 1984
Jan 1988
Jan 1992
Jan 1996
Jan 2000
Jan 2004

Figure 11

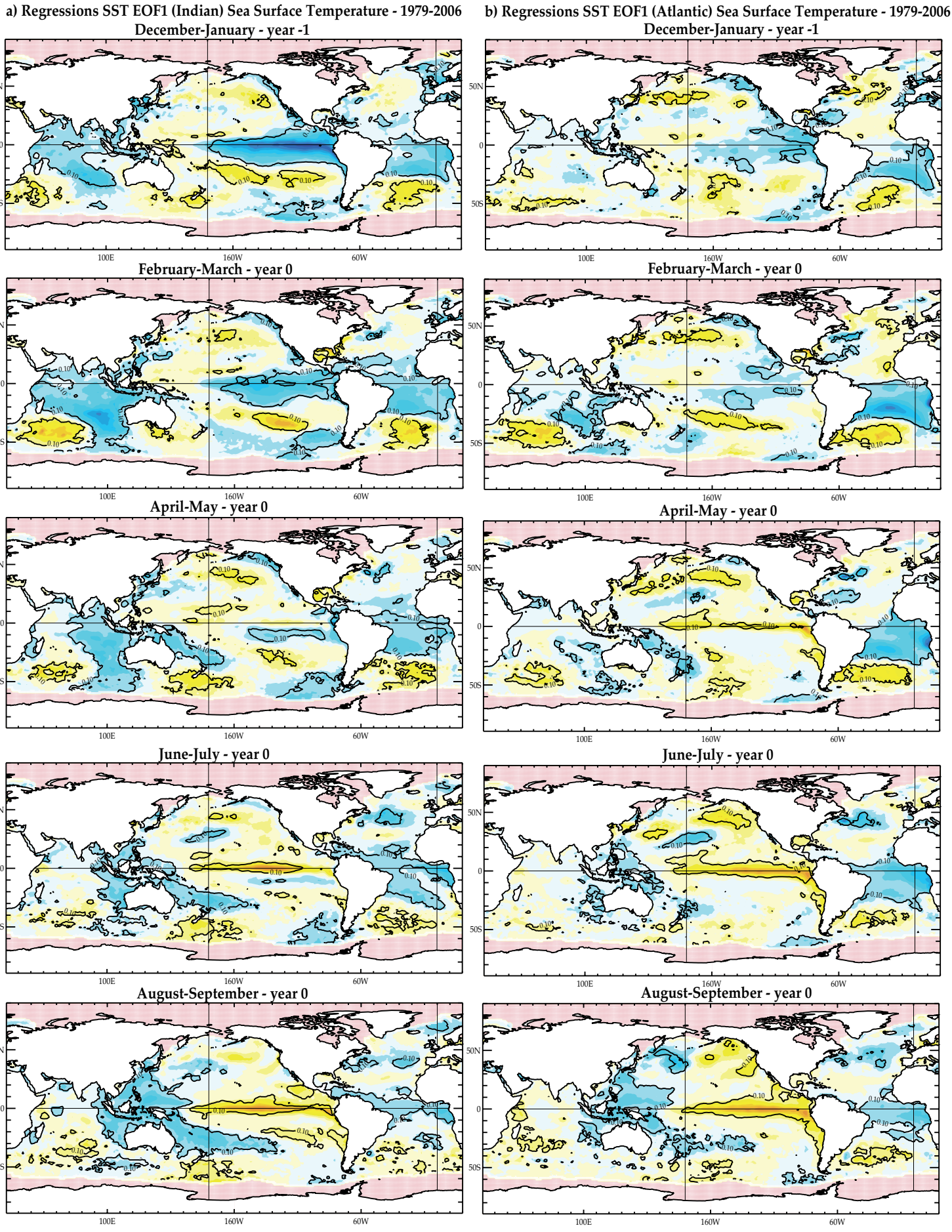
a) Regressions SST EOF1 (Indian) Sea Surface Temperature - 1979-2006
December-January - year -1
February-March - year 0
April-May - year 0
June-July - year 0
August-September - year 0
b) Regressions SST EOF1 (Atlantic) Sea Surface Temperature - 1979-2006
December-January - year -1
February-March - year 0
April-May - year 0
June-July - year 0
August-September - year 0
50N
0
50S
100E
160W
60W
-1.0 -0.8 -0.6 -0.4 -0.2 0.0 0.2 0.4 0.6 0.8 1.0
degree C by STD

Figure 12

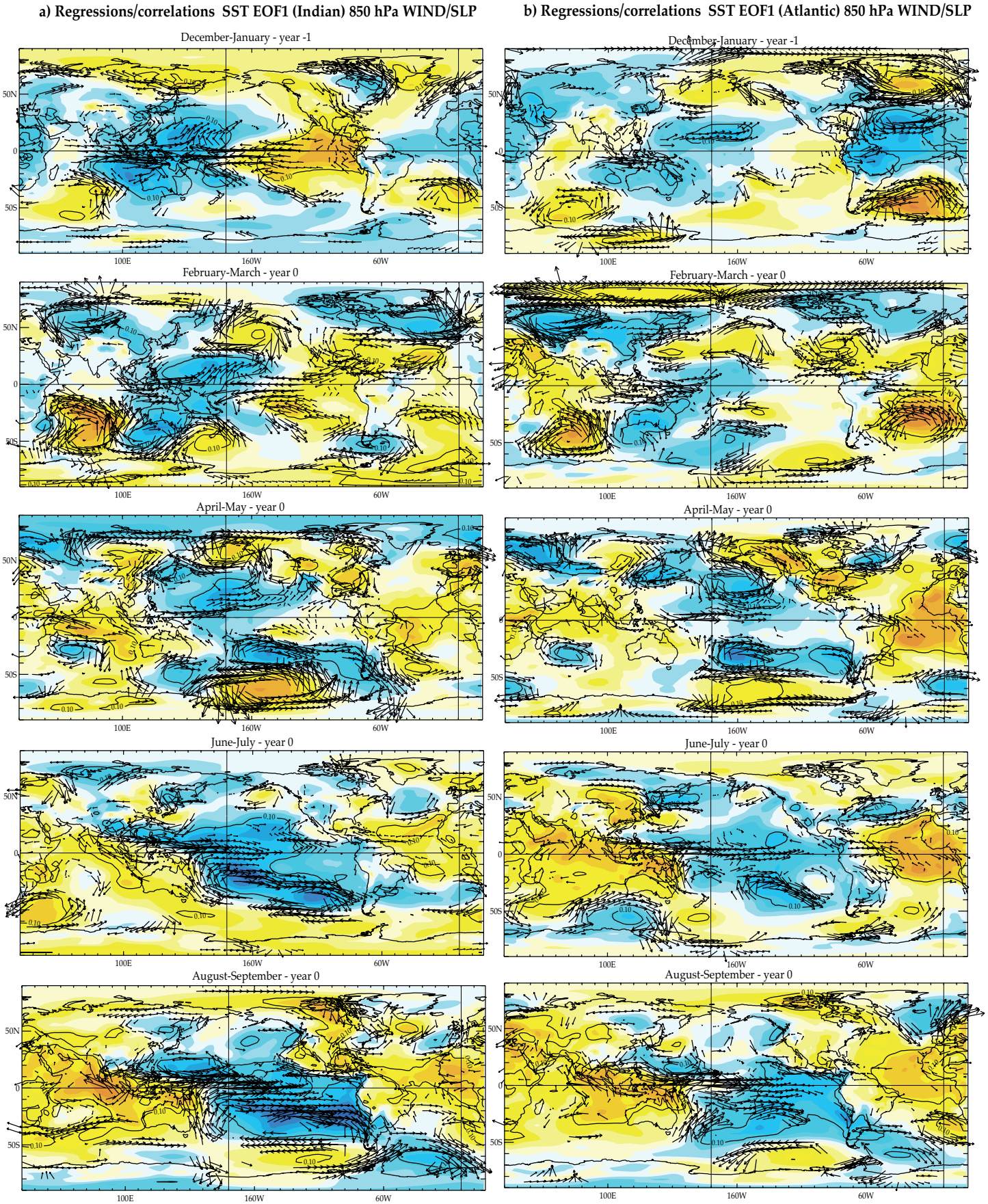
a) Regressions/correlations SST EOF1 (Indian) 850 hPa WIND/SLP
b) Regressions/correlations SST EOF1 (Atlantic) 850 hPa WIND/SLP
December-January - year -1
February-March - year 0
April-May - year 0
June-July - year 0
August-September - year 0
50N
0
50S
100E
160W
60W
1 m/s by STD
-1.00 -0.80 -0.60 -0.40 -0.20 0.00 0.20 0.40 0.60 0.80 1.00
CORRELATION

Figure 13

a) Regressions SST EOF1 (Indian) OLR - 1979-2006

b) Regressions SST EOF1 (Atlantic) OLR - 1979-2006

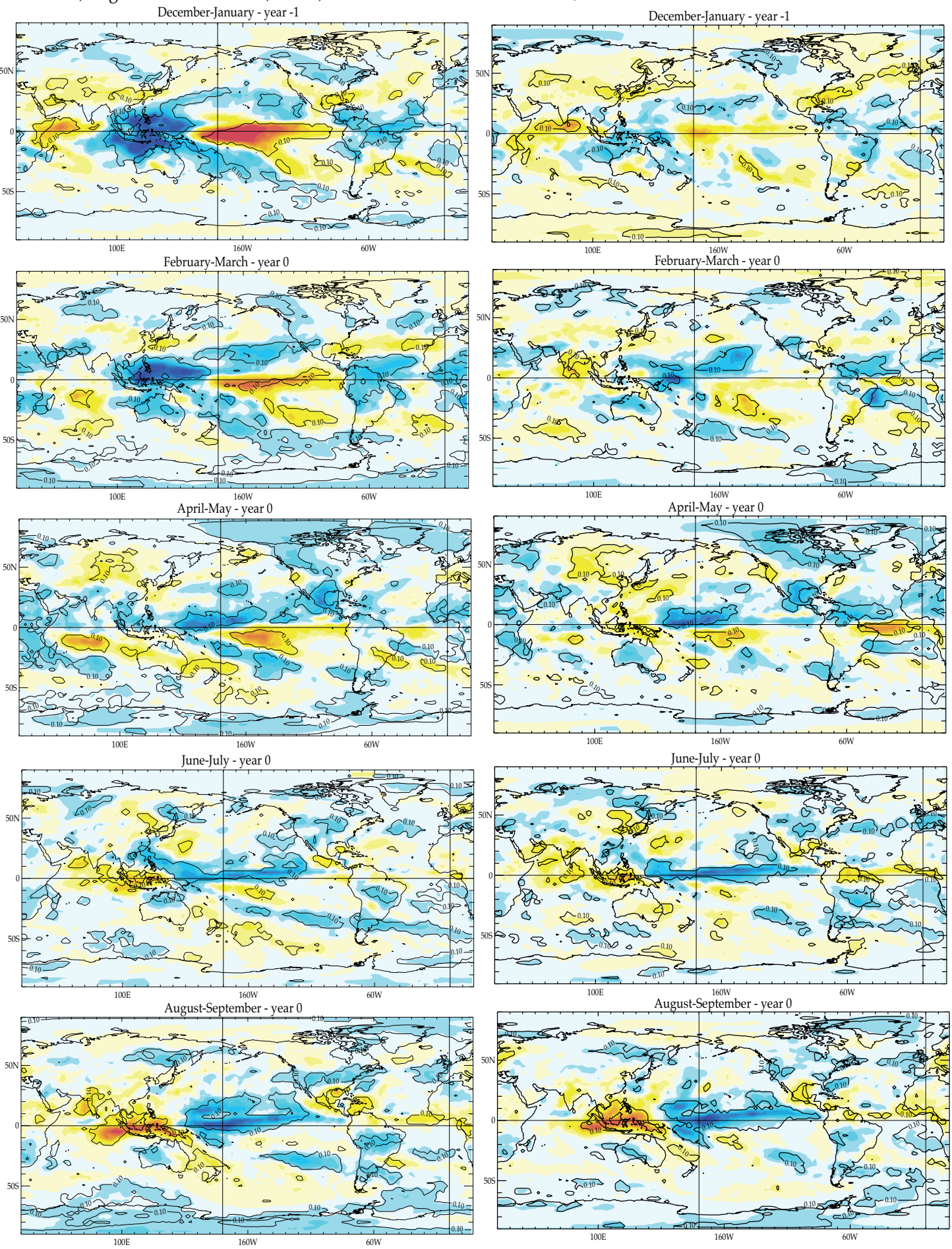

Figure 14

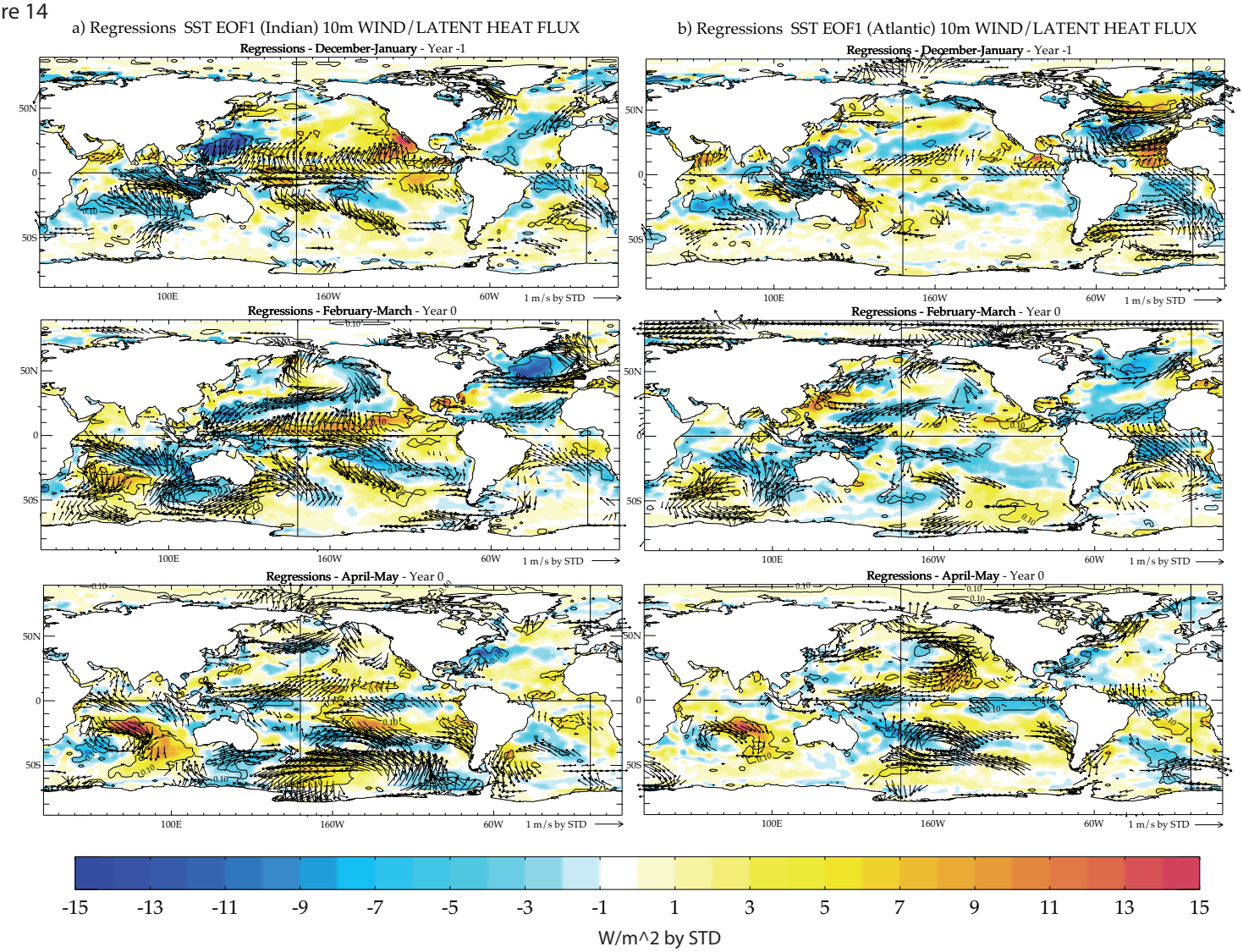
a) Regressions SST EOF1 (Indian) 10m WIND/LATENT HEAT FLUX
b) Regressions SST EOF1 (Atlantic) 10m WIND/LATENT HEAT FLUX
Regressions - December-January - Year -1
Regressions - February-March - Year 0
Regressions - April-May - Year 0
50N
0
50S
100E
160W
60W
1 m/s by STD
-15 -13 -11 -9 -7 -5 -3 -1 1 3 5 7 9 11 13 15
W/m^2 by STD

Figure 15

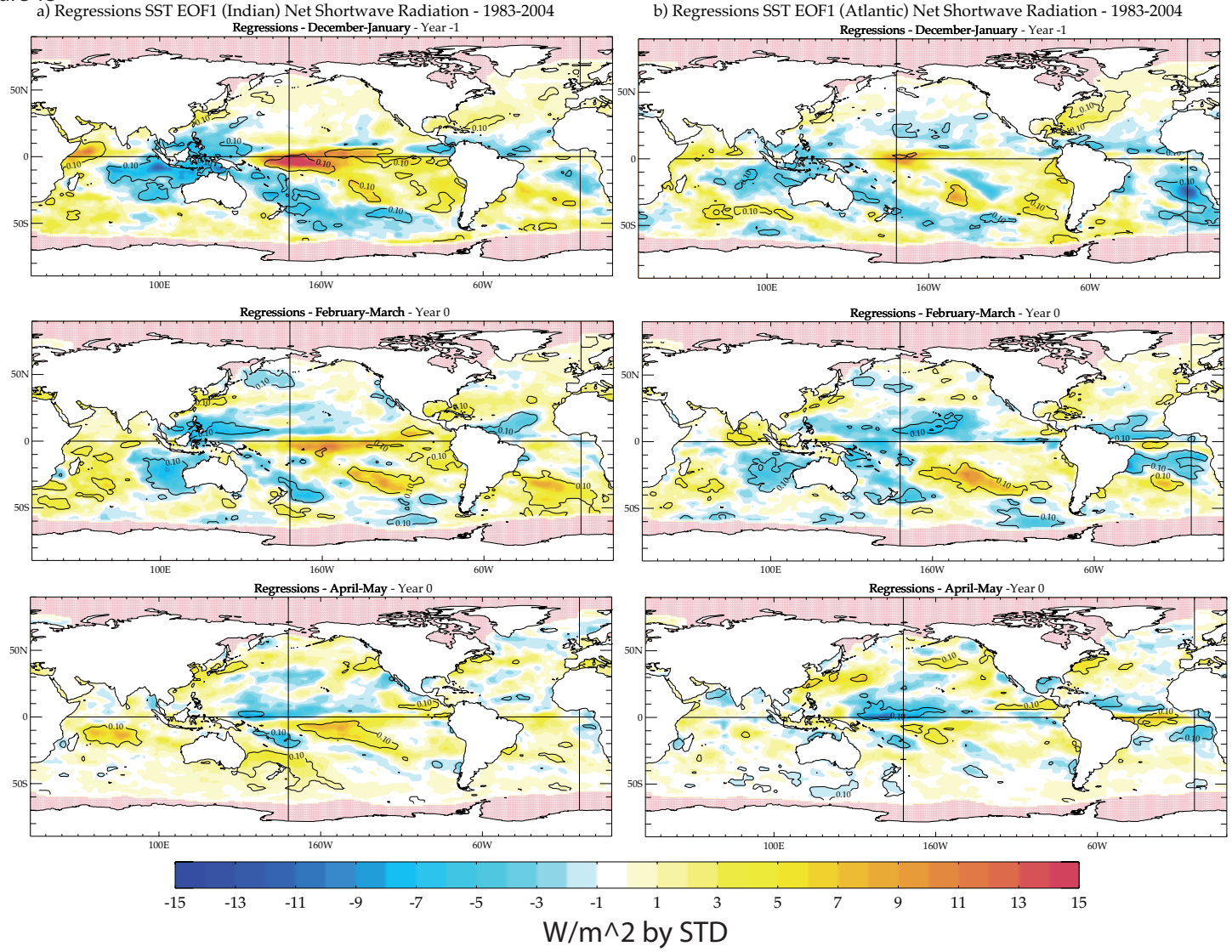
a) Regressions SST EOF1 (Indian) Net Shortwave Radiation - 1983-2004
b) Regressions SST EOF1 (Atlantic) Net Shortwave Radiation - 1983-2004
Regressions - December-January - Year -1
Regressions - December-January - Year -1
Regressions - February-March - Year 0
Regressions - February-March - Year 0
Regressions - April-May - Year 0
Regressions - April-May -Year 0
50N
0
50S
100E
160W
60W
-15 -13 -11 -9 -7 -5 -3 -1 1 3 5 7 9 11 13 15
W/m^2 by STD

Figure 16

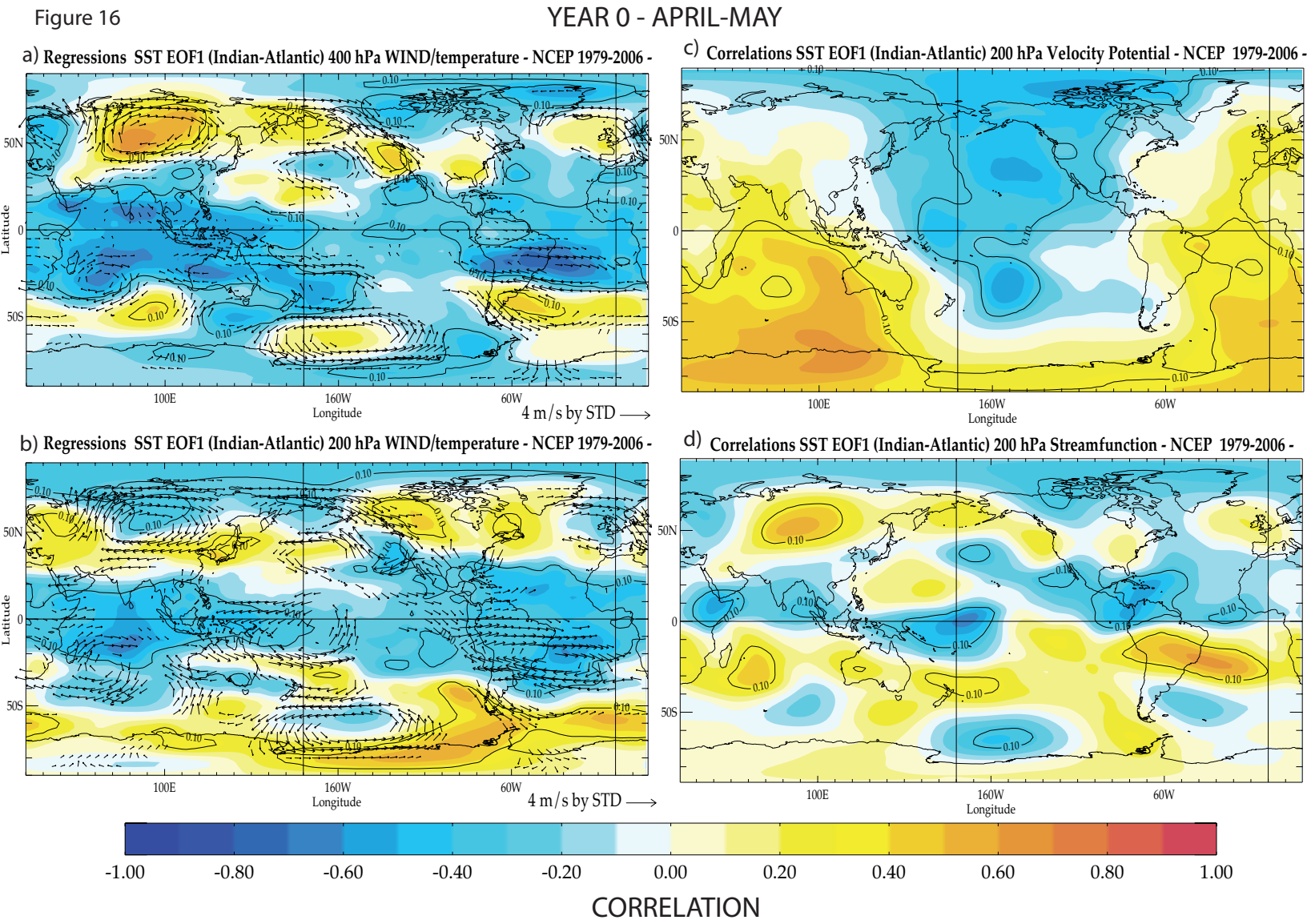
YEAR 0 - APRIL-MAY
a) Regressions SST EOF1 (Indian-Atlantic) 400 hPa WIND/temperature - NCEP 1979-2006 -
c) Correlations SST EOF1 (Indian-Atlantic) 200 hPa Velocity Potential - NCEP 1979-2006 -
b) Regressions SST EOF1 (Indian-Atlantic) 200 hPa WIND/temperature - NCEP 1979-2006 -
d) Correlations SST EOF1 (Indian-Atlantic) 200 hPa Streamfunction - NCEP 1979-2006 -
50N
0
50S
Latitude
100E
160W
60W
Longitude
4 m/s by STD
-1.00
-0.80
-0.60
-0.40
-0.20
0.00
0.20
0.40
0.60
0.80
1.00
CORRELATION

Figure 17

Potential Temperature equatorial cross-section regressions - year 0 -

a) SST EOF1 Indian

b) SST EOF1 Atlantic

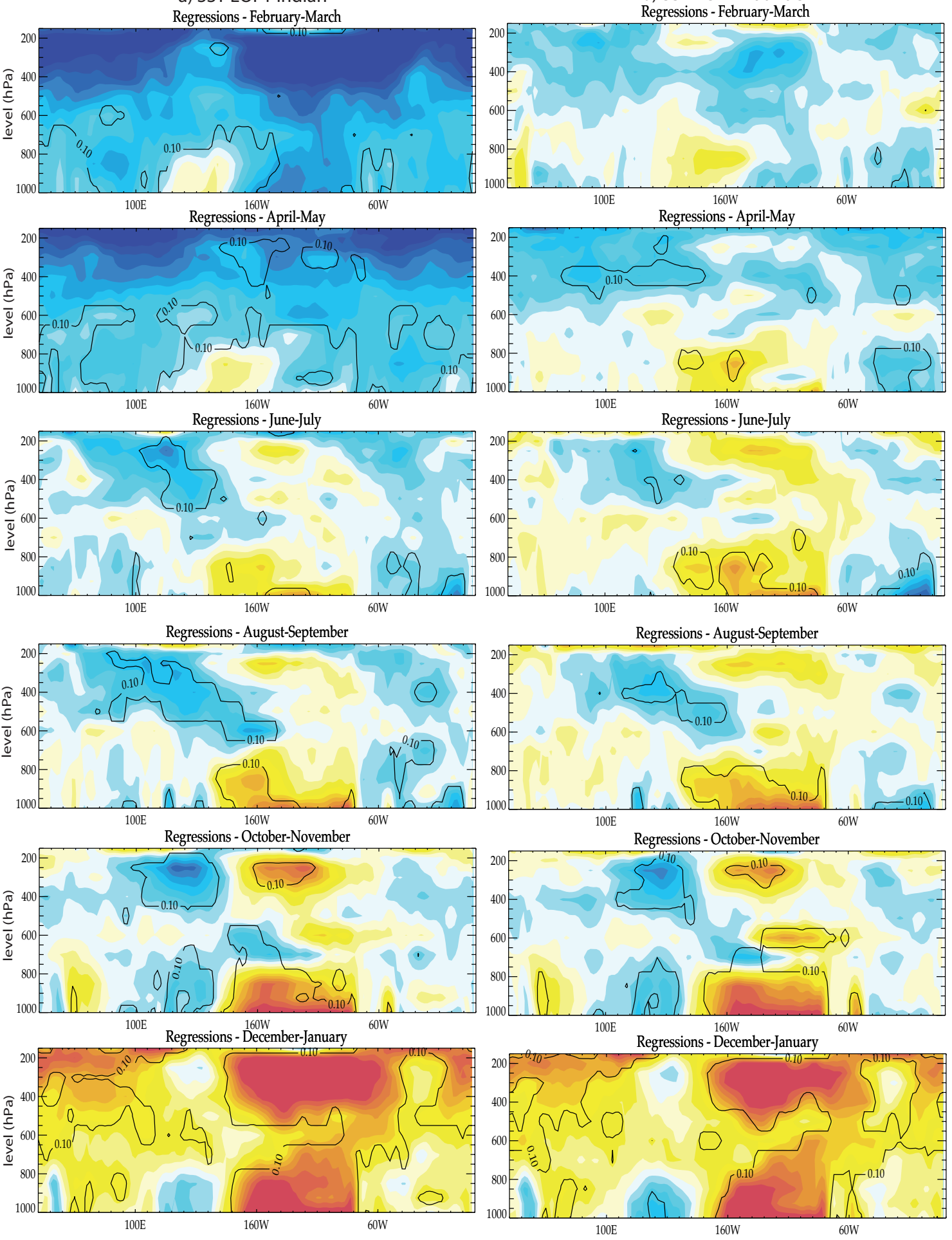

latitudes in [-4.0, 4.0] - (3 points)

degK by STD

-0.50 -0.40 -0.30 -0.20 -0.10 0.00 0.10 0.20 0.30 0.40 0.50